



THE UNIVERSITY of EDINBURGH
School of Physics
and Astronomy

Effects of substrate wettability on the evaporation dynamics of drying suspension droplets containing colloidal silica particles

MPhys Project Report

Theo Reid

Submitted for the 40pt MPhys Project course PHYS11016
September 19, 2023

Abstract

The evaporation of a particle-laden droplet leading to the formation of a ring-like deposit is a phenomenon ubiquitous in nature, it is known as the “coffee ring effect”. These ring-like deposits have implications in industrial processes such as ink-jet painting and the construction of nanomaterials, and thus there have been many attempts to control the evaporation processes that dictate the shapes of the deposits formed. In this project, the effect of surface wettability on the internal flows within evaporating sessile droplets and the resultant dried deposits are investigated. By imaging colloidal silica droplets evaporating on three different surfaces, we observe how surface wettability affects droplet evaporation dynamics. For the high wettability substrate, untreated glass, we observe large outward flows towards the contact line near the base of the droplet and large inward flows towards the centre of the droplet near its apex. For lower wettability substrates, plastic and silanised glass, we observe low velocity inward flows at all heights within the droplets. Moreover, we observe that the strength of the coffee ring formed increases with wettability. The project demonstrates that surface wettability has significant effects on the evaporation dynamics of evaporating sessile droplets and their resultant dried deposits.

Supervisor: Dr Job Thijssen

Personal statement

The first couple of weeks involved reading literature related to my research project and devising a plan to adhere to over the course of the year. The plan covered key deadlines throughout the year and included projected dates for tasks such as: completing lab safety and microscope training, running dummy trials for the microscopy experiments, and collecting an initial set of results to use for data analysis. At this point in time, I had not completed the health and safety forms nor the lab training so I focused on familiarising myself with some of the analysis techniques that I would later be using. A significant portion of the image analysis in this project was carried out using FIJI (*FIJI is just ImageJ*), so I tried to use this time to learn the software. I used practice data provided by my supervisor to explore particle tracking with Trackmate, a FIJI plugin. Furthermore, I began to write Python code which would allow me to convert the outputted CSV files from my analysis in FIJI into Pandas data frames that I could analyse in Python.

By week four I had acquired an understanding of much of the physics behind what causes the coffee ring effect. I knew that eventually, I would be characterising the strength of the coffee ring formation from bright-field images, so I began to research different methods of deposit characterisation in addition to writing code that would calculate the κ and ζ parameters. Once my health and safety forms were complete, I arranged various training sessions required for me to be allowed to operate in the lab and use the necessary equipment for my project. The confocal microscope training took the most time due to the complexity of the software. There were several small details that were essential to set up the microscope for my intended use and so I found myself referring to notes taken during this training frequently throughout the year. In addition, I underwent general lab training and laser training, and I was taught how to operate the bright-field microscope by my supervisor. Over the next few weeks, I spent my time in the lab cleaning my fluorescent colloid sample to remove the dye from the water. This meant completing cleaning cycles as frequently as possible. I was very grateful that my supervisor was able to help with this process by completing additional cleaning cycles as well as checking the colour and PH of the supernatant. While this cleaning procedure was taking place, I carried out some initial experiments on a sample of colloidal silica with no fluorescent dye. For example, I tested for the concentration of silica particles in water that would result in the strongest coffee ring formation when a drop of the dispersion was evaporated on a glass substrate.

The final couple of weeks of the first semester involved biosafety training for the CAT2 labs, training to use the tensiometer and taking initial results with both the bright-field and confocal microscopes. I also spent time researching circle fits, specifically Hough transforms and how I could utilise them to calculate the centres and radii of the evaporated droplet deposits. In the first week of semester two, I developed code for the ζ parameter, which I would use to characterise the final deposits from bright-field images. Due to my confusion around the ζ parameter, as well as exploring different methods of characterisation, this process took significantly longer than I had anticipated (I finalised my code for deposit characterisation in week 7). Unfortunately, the initial confocal images I had taken in Semester 1 were overcrowded with fluorescent silica particles, making it challenging to track individual particles.

Over the next couple of weeks, I adjusted the concentration of the fluorescent colloidal dispersions in an attempt to find a balance that would allow for individual particle tracking. During this time I took contact angle measurements for the different substrates. Additionally, I encountered an issue with my parafilm substrate scattering the confocal microscope laser and so I opted to substitute parafilm with another substrate with low wettability: silanised glass. This meant learning how to silanise glass with silanisation solution 1 as well as taking more contact angle measurements for my new substrate. I also went back and took bright-field images with the silanised glass substrate so that I had a complete set of confocal and bright-field images for three substrates: untreated glass, plastic and silanised glass. The contact angle measurements were quite time-consuming since the Drop Shape Analyser software would have the tendency to crash mid-way through droplet evaporation. Moreover, the computer would sometimes have to be restarted several times for the software to work. Together with the popularity of the tensiometer, making it difficult to book a slot, these issues made the desired contact angle measurements difficult to take.

In the following few weeks, I managed to complete my confocal microscope measurements and began the image analysis for the project. This involved delving further into FIJI, since my results were not as clean as the practice data I had used for particle tracking in Semester 1. The last few weeks of the project were dedicated to further background research, finishing my data analysis and writing my report,

Acknowledgments

I would like to thank my supervisor Dr Job Thijssen for the guidance and support that he has provided throughout this project. I would also like to extend this gratitude to Dr Andrew Schofield, Dr John Royer and Dr Andreia da Silva for their assistance and training in the labs. Finally, I wish to thank the members of the Evaporation on complex surfaces team who provided feedback on my research throughout the year, as well as broadening my knowledge of the field.

Contents

1	Introduction	1
2	Background	2
2.1	Colloids	2
2.1.1	Interaction forces between colloidal particles	3
2.1.2	Gravitational effects on colloidal particles	5
2.1.3	Brownian motion	6
2.2	Droplet evaporation	7
2.3	Substrate wettability	9
3	Materials and Methods	10
3.1	Materials	10
3.2	Overview	10
3.3	Colloid preparation	11
3.4	Substrates	11
3.5	Drop shape analysis	11
3.6	Bright-field microscopy	13
3.7	Characterising the Deposit	14
3.8	Fluorescent microscopy	16
3.9	Particle tracking	17
4	Results and Discussion	19
4.1	Dried deposits	19
4.2	Drop shape analysis	23
4.3	Flow of particles	25
5	Conclusion	32

1 Introduction

When a particle-laden droplet evaporates on a surface, it can leave a ring-like pattern due to a higher concentration of deposited particles at the perimeter of the droplet than at the centre. The shape of the deposit has implications for manufacturing processes such as inkjet printing [1],[2],[3], the formation of colloidal crystals [4],[5], and the construction of functional nanomaterials [6],[7]. It can also have detrimental effects on commercial applications such as fluorescent microarrays [8],[9], surface-enhanced Raman spectroscopy [10],[11] and matrix-assisted laser desorption/ionisation spectrometry [12],[13].

R.D. Deegan et al. attributed the coffee ring effect to contact line hysteresis and capillary flow outward towards the edge of the droplet during evaporation [14]. They demonstrated that for a particle-laden droplet with a fixed contact line (the triple-phase boundary), evaporation flux diverges at the perimeter due to the larger liquid-vapour interface at the droplet perimeter compared to the interface at the apex of the droplet. To replenish this lost liquid at the droplet edge, an outward capillary flow is induced. This moves particles to the edge of the droplet where they are deposited, causing a ring-like stain on the surface. A plethora of research has been carried out to gain an understanding of what factors affect the shape of the deposit formed and how the coffee ring can be suppressed. In 2017, Das et al. showed that they could avoid the ring-like stain when evaporating a colloidal suspension droplet on a glass surface by coating the surface in a thin layer of silicone oil. The coating prevented the contact line pinning and caused a lower initial contact area which resulted in a decreased surface area and therefore lower evaporation rate. These effects combined to produce a uniform deposit [15]. Another method of suppressing the coffee ring effect involves using ellipsoidal particles which have strong interparticle attractions, thus aggregating more readily. This leads to the formation of a loosely packed structure at the liquid-vapour interface, which resists the outward radial capillary flow that would carry the particles to the contact line [16]. Bansal et al. showed that the coffee ring effect could be suppressed by increasing colloidal particle diameters causing significant gravimetric settling which results in a uniform deposit [17]. Using a diffusion-limited cluster-cluster aggregation (DLCA) simulation model, Crivoi et al. demonstrated that particle sticking probability was a crucial factor in the morphology of the dried deposits. They showed that adding surfactant inside a water suspension of aluminium oxide nanoparticles would result in a coffee ring deposition where typically, one would observe a uniform deposit [18]. While the popular approach to suppressing the coffee ring effect involves depinning the contact line, Hu et al. observed that Marangoni flow may also need to be suppressed. Driven by surface-tension gradients produced by the latent heat of evaporation, Marangoni flow can reinforce or counteract (depending on the relative surface, liquid and vapour properties) outward radial capillary flow which can alter the shape of the deposit [19].

Significant efforts have gone into researching how droplet composition can affect deposit formation, but there has been less focus on the effects of the substrate properties. A 2021 preprint by C.M. Perez et al. outlines a systematic approach to investigating the effect of surface wettability on the evaporation dynamics near the base of a particle-laden droplet using both image analysis techniques and mathematical modelling [20]. This project aims

to provide additional experimental data for the publication of this preprint by exploring the evaporation dynamics at different heights within evaporating particle-laden droplets. To achieve this, two different methods of imaging are used. The first of which involves using bright-field microscopy to characterise the dried deposits of evaporated colloidal silica on substrates of varying wettability, determined by the initial contact angle, CA_i , between the substrate and the droplet surface. The aim of this is to relate the wettability of a substrate to the strength of the coffee ring formation, in a quantifiable way. The second stage involves using confocal microscopy to observe the movement of particles at different heights within evaporating droplets. Crucially, the confocal microscope allows for imaging of focal planes which can be stacked to create 3D visualisations of the evaporating droplet flows. By carrying out the experiment in this two-stage process, we are able to first verify results from the preprint, and then provide insight into evaporation dynamics at different heights within the droplet to formulate a more complete picture of how substrate wettability affects the deposition of particles during the evaporation of particle-laden droplets.

2 Background

A sessile droplet describes a drop residing on top of a horizontal surface [21]. In 1977, Picknett and Bexon distinguished two modes to model evaporating sessile droplets: the constant contact radius (CCR) mode and the constant contact angle (CCA) mode (see figure 1). CCR evaporation occurs when the contact line is pinned such that it does not recede as the droplet evaporates. This creates a distinct wedge-shaped droplet. CCA evaporation is when the contact line recedes, keeping the contact angle fixed as the droplet shrinks [22].

There are many factors that affect the contact line dynamics and resultant dried deposits for evaporating sessile droplets including droplet composition [16], surface properties [24] and the presence of surfactants [18]. The mechanisms involved in the evaporation of colloidal suspensions are discussed below.

2.1 Colloids

A colloidal dispersion is a heterogeneous system in which one insoluble substance is dispersed throughout another substance. A colloid has a continuous phase (the medium of suspension) and a dispersed phase (the suspended particles, with sizes typically between approximately 10 nm and several microns [25]). Colloidal dispersions are characterised by a very high interfacial area which corresponds to large interfacial energy. In order to reduce this energy, the particles aggregate. However, this aggregation is sometimes prevented due to the stability of the colloidal dispersion.

Gravity is one force that affects the stability of a dispersion. If the dispersed particles are denser than the dispersion medium, they sediment. If they are less dense than the dispersion medium, they rise. With small enough particles, the effects of gravity are minimised, and

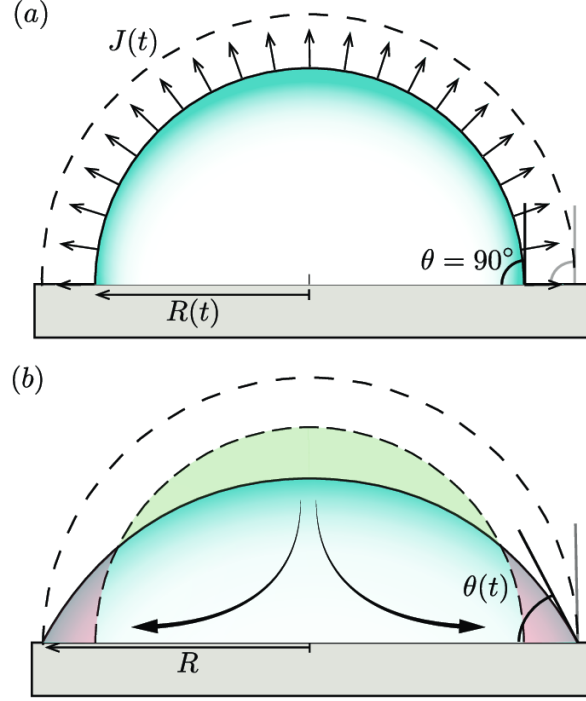


Figure 1. A sessile droplet evaporating uniformly with evaporation flux $J(t)$ and with an initial contact angle of $\theta = 90^\circ$. In (a) the droplet evaporates with a constant contact angle (CCA) and the contact line recedes. The liquid air interface moves from the dashed contour to the solid contour. In (b), the contact line is pinned such that there is a constant contact radius as the droplet evaporates, displayed by the solid contour. To maintain its spherical cap shape dictated by surface tension, outward capillary flows move liquid from the centre of the droplet to the contact line, compensating for the evaporated liquid [23].

so other mechanisms must be considered. One such mechanism is Brownian motion; the random movement of particles in a fluid resulting from bombardment from molecules of the surrounding medium [26]. There are also interaction forces between the colloidal particles that are crucial in understanding colloidal suspensions.

2.1.1 Interaction forces between colloidal particles

The Van der Waals force is a weak attractive force that exists between neighbouring particles, it arises from fluctuations in the dipoles of the particles. Typically, Van der Waals forces are described as a net force due to contributions from London dispersion forces (fluctuating dipole-induced dipole forces), Debye forces (interactions between rotating permanent dipoles and induced dipoles), and Keesom forces (electrostatic interactions between rotating permanent dipoles, quadruples and multipoles) [28]. The Van der Waals interaction energy, W_{VdW} , for two spherical particles both with radius R and a separation D is given by equation 1 [29].

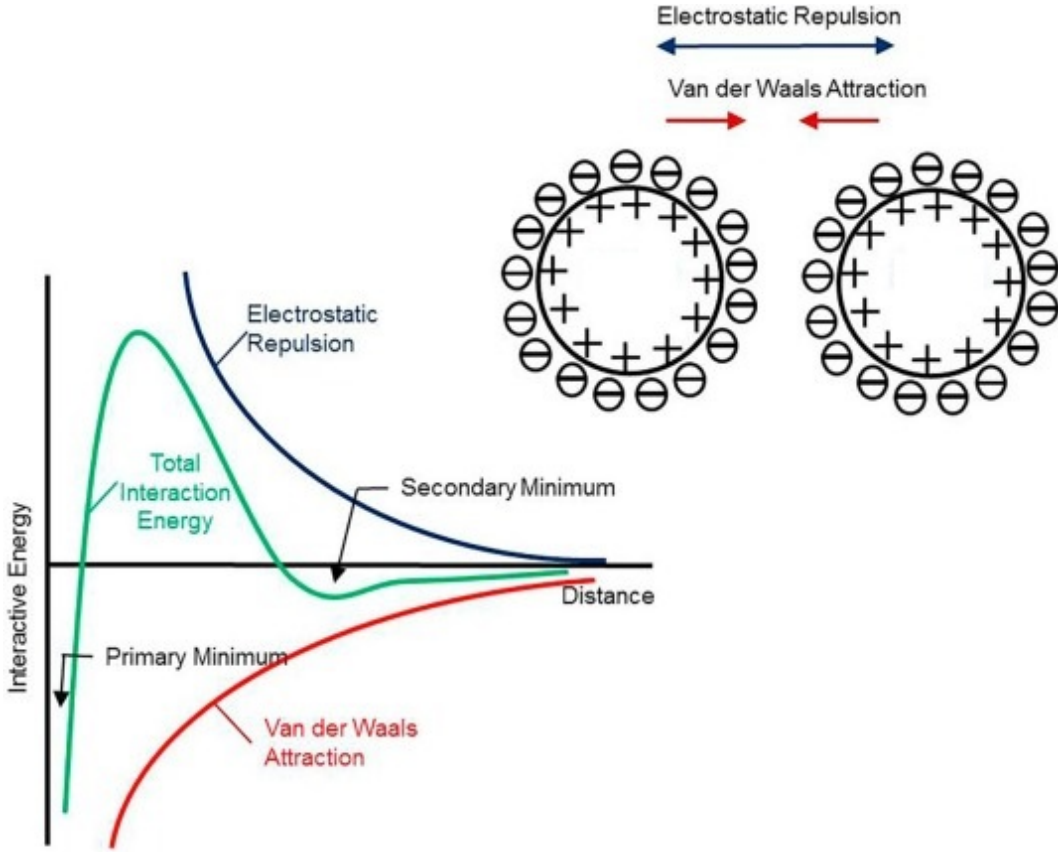


Figure 2. DLVO theory. A diagram of the Van der Waals attraction and electrostatic repulsion for colloidal particles [27].

$$W_{VdW} = \frac{AR}{12D} \quad (1)$$

Where A is the Hamaker constant which depends on the relative dielectric constants between the particles and the medium.

There are two primary ways in which the aggregation of colloidal particles is opposed. The first of which is electrostatic stabilisation which describes the balancing of Van der Waals forces by coulomb interactions between charged particles. For colloids dispersed in a medium, the electric double layer has an important role in electrostatic stabilisation. Negatively charged ions in the medium are adsorbed to the surface of a particle, creating a negative surface charge. This causes a layer of positive ions to surround the particle forming an electric double layer that repels other particles as shown in figure 3. Another mechanism for stabilisation is steric stabilisation. This refers to the effects of adsorbed layers of surfactant molecules on the surface of colloidal particles. These layers create a repulsive barrier between the particles, preventing the particles from aggregating and thus help to maintain the stability of colloidal suspensions [30]. The colloidal particles in this experiment were charge stabilised. Hence, DLVO theory, established by Derjaguin, Landau, Verwey, and Overbeek,

is important for understanding the dried deposit formations. DVLO theory describes the forces between colloidal particles as the sum of the Van der Waals force and the electric double-layer force (figure 2). It is assumed that the electrostatic double layer forces and the Van der Waals forces act independently and DLVO theory is generally a good estimation for intersurface forces down to surface separations of approximately 5 nm [31].

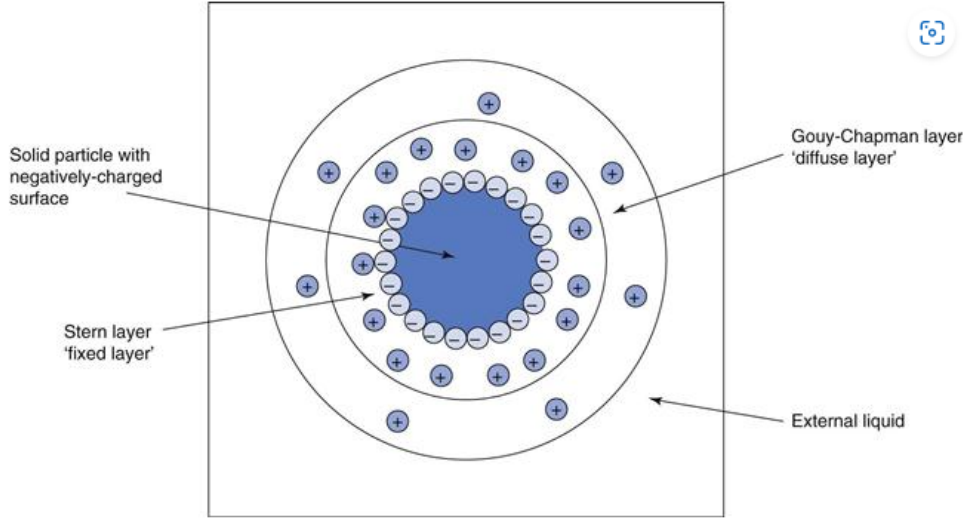


Figure 3. The electric double layer for a solid particle suspended in a liquid medium [32].

2.1.2 Gravitational effects on colloidal particles

In addition to interactions between neighbouring particles, colloidal particles will also experience forces exerted by the surrounding fluid. A spherical object in a fluid medium accelerating under gravity will experience an opposing drag force until the object reaches a terminal velocity. The mechanism behind this force relies on the Reynolds number, a ratio between inertial and viscous forces [33]. For a spherical object, radius a , moving with velocity v through a medium of viscosity η and density ρ , the Reynolds number is given by:

$$Re = \frac{\rho v a}{\eta} \quad (2)$$

For colloidal particles dispersed in water, this value is very low. In this regime, Stokes law is applicable for describing the drag force. The drag force and force due to gravity can be equated to give the terminal velocity of a particle accelerating through a fluid under gravity. The drag force and the gravitational force on a single particle as well as its terminal velocity are given by equations 3, 4 and 5 respectively [34].

$$F_s = 6\pi\eta av \quad (3)$$

$$F_g = \frac{4}{3}\pi a^3 \Delta\rho g \quad (4)$$

$$v_t = \frac{2a^2 \Delta\rho g}{9\eta} \quad (5)$$

Where F_s is the drag force, F_g is the gravitational force, g is the gravitational acceleration and $\Delta\rho$ is the difference between the particle and medium densities.

Typically, for colloidal particles below 1 μm in diameter, the gravitational effects are assumed negligible since they are dominated by diffusive motion [35] [36]. A study in which atomic force microscopy measurements were used to investigate the effect of gravity on colloidal particles showed that gravity has an appreciable effect on colloidal particle deposition even with particles smaller than 100 nm. However, they concluded that gravitational effects were only non-negligible at these scales for high-density particles such as colloidal gold, which has a density of 19.3 g/cm^3 [37]. In comparison, the silica colloidal particles used in this experiment are approximately 2 g/cm^3 , so gravity should not affect the particle deposition here.

2.1.3 Brownian motion

In 1827, while examining pollen grains, Robert Brown observed that small particles that had ejected from the grains would undergo random irregular motion in water [38]. Einstein argued that this motion is clear evidence for the atomic nature of matter and that the mean-squared displacement (MSD) of colloidal particles is the primary observable quantity [39][40].

The probability density function to describe Brownian particles can be determined using the MSD. The 1D MSD for a colloidal particle undergoing a dissipative drag force, $-\mu v$ (where μ is the drag coefficient), and impulses from surrounding liquid molecules is given by:

$$MSD = \frac{d\langle x^2 \rangle}{dt} = \frac{2KT}{\mu} t \quad (6)$$

where K is the Boltzmann constant, T is the temperature and t is time. Using Stokes' law (equation 3), this can be rewritten as:

$$MSD = \frac{2KT}{6\pi\eta a} t \quad (7)$$

where a is the radius of the spherical particle and η is the medium viscosity. By defining the self-diffusion constant, $D = \frac{KT}{6\pi\eta a}$, equation 7 can be expressed more simply as:

$$MSD = 2Dt \quad (8)$$

This derivation can be scaled to n dimensions following the same argument. Hence, in 2D the MSD can be defined as:

$$MSD = \langle R^2 \rangle = 4Dt \quad (9)$$

This is very small for particles on the scale of a micrometre dispersed in water at room temperature. Therefore, in this project we consider the movement of particles to be predominantly caused by internal flows within the droplets. However, Brownian motion still has the effect of stabilising colloidal suspensions by dominating gravitational effects on the particles. This allows us to neglect sedimentation in our treatment of colloidal particles [41].

2.2 Droplet evaporation

The ring-like deposit formed due to the evaporation of a sessile droplet is influenced by contact line pinning and contact angle hysteresis [42].

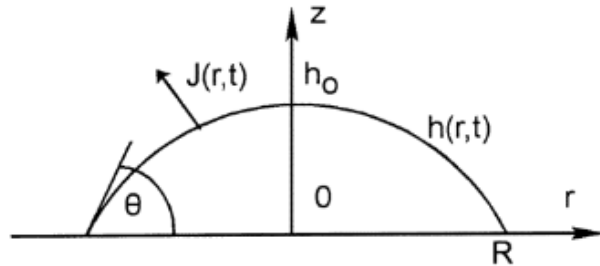


Figure 4. Droplet with a spherical cap shape resting on a flat surface. θ is the contact angle, $h(r,t)$ is the local height and $J(r,t)$ is the local evaporation flux [43].

There are different modes of evaporation that can affect the formation of a coffee ring. In one mode, the contact line is pinned. Figure 4 illustrates a circular droplet of fixed radius, R , an initial height, h_0 , and decreasing contact angle, θ , drying on a solid surface. The evaporation flux $J(r,t)$ affects the height profile, $h(r,t)$ across the droplet. At the perimeter of the droplet, the liquid would evaporate entirely causing the droplet to shrink in radius, however since the contact line is pinned, there must be an outward radial flow to compensate for the liquid lost at the perimeter [14].

Two sources of convective flow within an evaporating droplet are buoyancy convection and capillary convection. Buoyancy convection is due to the vertical temperature gradient inside a droplet [44]. Typically, buoyancy convection is characterised by the Rayleigh number:

$$Ra = \frac{g\beta}{\eta\alpha}(T_s - T_\infty)l^3 \quad (10)$$

where g is the acceleration due to gravity, β is the coefficient of thermal expansion, η is the kinematic viscosity, α is the thermal diffusivity, T_s is the temperature at the droplet surface, T_∞ is the temperature far away from the surface and l is the height of the drop in the case of a sessile drop. Buoyancy convection arises in pendant droplets but is seen less in sessile droplets [14]. It has been observed to play a significant role in the evaporation of sessile droplets on superhydrophobic surfaces ($CA_i > 150^\circ$), however in this experiment, the highest contact angle measured was 101.6° , so the effects of buoyancy convection are limited. Another source of convective flow arises from the Laplace pressure as the drop shape evolves during evaporation. Cohesive forces between molecules in the droplet create surface tension, γ , at the liquid-vapour interface. For a droplet with a radius of curvature R , the Laplace pressure is defined as:

$$\Delta P = P_i - P_o = \frac{2\gamma}{R} \quad (11)$$

where P_i is the pressure inside the droplet, and P_o is the pressure outside the droplet. This pressure drives convective flow in the droplet. Competition exists between the Laplace pressure and pressure due to gravity, $P_g = 2\rho g R$, where the height of the droplet is $2R$. A capillary length can be defined by balancing these two pressures (equation 12).

$$\kappa = \sqrt{\frac{\gamma}{\rho g}} \quad (12)$$

Where ρ is the density of the droplet and g is the acceleration due to gravity. For water droplets on Earth, this is on the scale of a millimetre [45]. Since the droplets used in this project are colloidal suspensions of silica particles in water, and are of similar scale, the balancing of Laplace pressure and gravitational pressure dictates the shapes of the droplets during evaporation.

When investigating the mechanisms behind coffee ring formation, another type of convective flow must be considered: Marangoni flow. This arises due to surface tension gradients often resulting from the temperature variation along the free liquid surface [46]. It occurs when surface tension forces dominate viscous forces [47]. The predominant theory is that for an evaporating sessile droplet, the evaporation flux diverges at the contact line because there is more available space at the edge of the droplet for evaporation [14] [48]. Non-uniform evaporative flux gives rise to a temperature gradient which leads to a surface tension gradient along the liquid-vapour interface, inducing Marangoni flow [49]. The Marangoni number characterises the strength of this convective flow, it is defined as:

$$Ma = \frac{\Delta\gamma R}{\nu\rho\alpha} \quad (13)$$

where $\Delta\gamma$ is the surface tension difference across the liquid-vapour interface, R is the radius of the spherical cap, ν is the kinematic viscosity, α is the thermal diffusivity and ρ is the liquid density. The presence of Marangoni flow does not necessitate an evolving drop shape. For example, if a sessile droplet resides on a substrate that is warmer than the surrounding vapour, the base of the droplet will be warmer than the apex region, inducing internal flows. Marangoni flow can also be caused by surface tensions due to the drop composition [50]. A non-uniform distribution of particles inside a droplet, which may occur due to outward capillary flows pushing particles to the droplet edge, causes a concentration gradient which can induce Marangoni flow [51].

2.3 Substrate wettability

Wettability is the ability of a liquid to spread over and adhere to a solid surface. Surface chemistry as well as surface forces are important in determining whether a droplet will wet a surface [52]. For a liquid drop residing on a solid surface in thermodynamic equilibrium, the surface tensions at the three-phase boundaries dictate the wetting. This is described by Young's equation which relates the equilibrium contact angle, θ_{eq} , and the surface tensions (γ_{sv} at the solid-vapour interface, γ_{sl} at the solid-liquid interface, and γ_{lv} at the liquid-vapour interface) [53]:

$$\gamma_{sv} = \gamma_{sl} + \gamma_{lv} \cos(\theta_{eq}) \quad (14)$$

From this equation, the wetting state can be obtained. Young described three distinct wetting states. One of which is complete wetting.

$$\gamma_{sv} = \gamma_{sl} + \gamma_{lv} \quad (15)$$

When the solid-vapour interfacial tension is equal to the sum of the solid-liquid and liquid-vapour surface tension, the droplet spreads out over the surface forming a film. The contact angle is zero in this case.

$$\gamma_{sv} < \gamma_{sl} + \gamma_{lv} \quad (16)$$

When the solid-vapour interfacial tension is less than the sum of the solid-liquid and liquid-vapour surface tension, we have partial wetting (described by equation 16) and the contact angle is less than 90° . The third state described by Young is non-wetting (described by equation 17). This occurs when the solid-vapour interfacial tension is greater than the sum of the solid-liquid and liquid-vapour surface tension, giving a contact angle greater than 90° .

$$\gamma_{sv} > \gamma_{sl} + \gamma_{lv} \quad (17)$$

Rarely when a drop is deposited on a solid surface will it be in equilibrium. In fact, a contact angle hysteresis is often observed, which is defined as the difference between the advancing contact angle and receding contact angle [54]. In this experiment, we predominantly observe a near-equilibrium initial state indicated by a pinned contact line, followed by a period of surface tension imbalance characterised by a moving contact line, and then a near-equilibrium state towards the end of evaporation.

3 Materials and Methods

3.1 Materials

A dispersion of silica particles (mean particle diameter 0.603 μm . Sigma-Aldrich) labelled with fluorescein isothiocyanate, functionalised by 3-aminopropyltriethoxysilane, and unlabelled silica particles (mean particle diameter 0.386 μm . Sigma-Aldrich) dispersed in distilled water (concentration 0.0002 wt% fluorescent particles and 0.4 wt% unlabelled particles) was used for all experiments carried out in this project.

Three substrates were used. A glass microscope slide (Cat No. 7101. Sail Brand. 25.4x76.2 mm. 1-1.2 mm thick.) cleaned with a paper towel soaked in ethanol ($\geq 99.8\%$, Sigma-Aldrich). A plastic Petri dish (Thermo Scientific. Sterilin. Standard 90 mm Petri dishes). A silanised glass microscope slide (Cat No. 7101. Sail Brand. 25.4x76.2 mm. 1-1.2 mm thick) functionalised with silanisation solution 1 ($\sim 5\%$ dimethyldichlorosilane in heptane, SelectophoreTM, Sigma-Aldrich).

3.2 Overview

This experiment consisted of two parts, both of which involved the imaging of particle-laden droplets evaporating on substrates of different wettabilities. The first part used bright-field microscopy to image the evaporation of droplets in order to explore the relationship between substrate wettability, measured by a droplet's initial contact angle, and the solid deposition after evaporation. The second part made use of a confocal microscope in order to image droplets at different heights during evaporation.

The droplet deposition technique was consistent across both parts of the experiment. A 2 μl droplet was deposited on a substrate using a micro-pipette held at an angle of approximately 30° from vertical. The micro-pipette was lowered down until the droplet touched the substrate, at which point the micro-pipette was slowly raised, leaving the droplet on the substrate. This technique was chosen because it allowed for the droplets to be deposited in the same manner for all of the substrates used.

3.3 Colloid preparation

For both the bright-field microscopy and confocal microscopy measurements, a dispersion of fluorescent and non-fluorescent silica particles in water was used as described in section 3.1. Before use, the fluorescent silica dispersion was cleaned in cycles. One cycle involved 30 minutes of sonication in a bath (VWR USC200T Ultrasonic Cleaner, frequency 45 kHz, maximum output power 120 W), 10 seconds of vortex mixing, followed by centrifugation for 60 minutes (Denley BS400 Centrifuge, 15 cm radius and 2100 RPM). The supernatant was then decanted and the tube containing the separated solid silica residue was filled with fresh, distilled water. This would then be placed on a roller bank to disperse the colloidal particles. The next cleaning cycle would commence only when there was no visible sediment in the tube. After 10 cycles, the supernatant appeared colourless and had a PH of 7 when measured using an indicator.

A concentration of 0.4 wt% silica in water suspension was found to be the ideal concentration for producing strong coffee rings. However, it was clear that this concentration of fluorescent silica particles would appear very crowded in confocal imaging, such that the individual particles could not be tracked. Hence, a dispersion of fluorescent and non-fluorescent silica particles was used.

3.4 Substrates

The aim of this experiment was to explore the relationship between substrate wettability and dried deposit patterns. Therefore, three different substrates with different initial contact angles were used: an untreated glass slide ($CA_i = 32.0 \pm 0.5^\circ$), a plastic Petri dish ($CA_i = 46.6 \pm 0.5^\circ$) and a silanised glass slide ($CA_i = 101.6 \pm 1.9^\circ$), where the initial contact angles were measured using a tensiometer. The method is outlined in section 3.5. The untreated glass and plastic substrates were cleaned with ethanol before use. The silanised glass was prepared by first cleaning a glass slide with ethanol before placing it in a plastic Petri dish and pouring the silanisation solution over it to completely submerge the slide. The Petri dish lid was placed on the dish and this was left for 10 minutes to allow for the reaction to take place. The slide was then removed from the Petri dish and rinsed with distilled water to clean it. The upward-facing side of the slide was used for droplet evaporation as this side was fully exposed to the silanisation solution, while the other side of the slide that was in contact with the Petri dish base was likely not fully coated.

3.5 Drop shape analysis

A Drop Shape Analyser (Krüss DSA100 drop tensiometer, model 65 FM40Mk2,) was used in combination with an Allied Vision Stingray camera to perform side-view imaging of the sessile droplets deposited on each of the three substrates (presented in figure 5). The Drop Shape Analyser software was used to measure the contact angles and base diameters during

the evaporation processes. The drop shape analyser has two main modes. The pendant drop method is an optical method for determining the surface tension or interfacial tension of a droplet, it utilises a Young-Laplace fit to the contour of a pendant droplet. This mode requires a pendant droplet which means that the droplet is suspended from a substrate. The second mode of operation is for determining the contact angle from the shadow image of a sessile droplet [55].

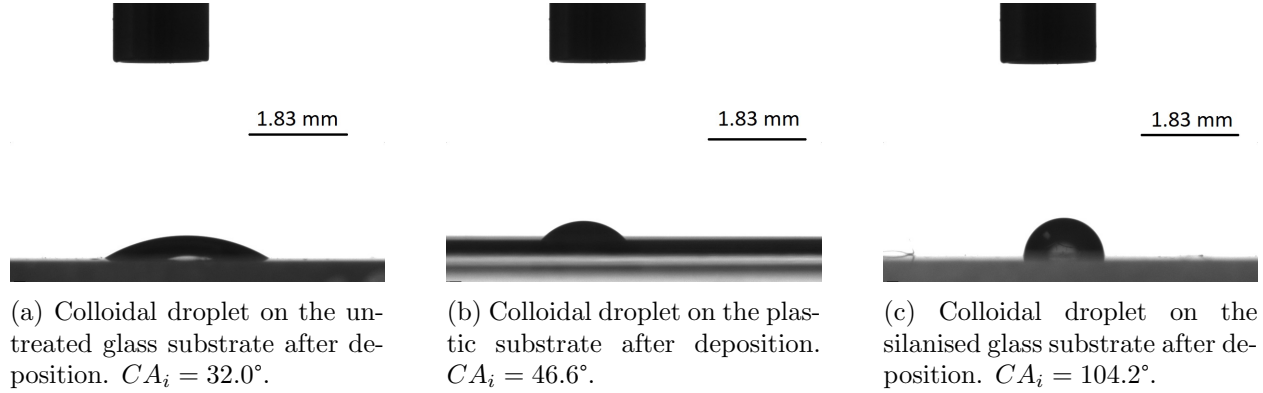


Figure 5. Side-view imaging of sessile droplets residing on the three different substrates.

To verify the accuracy of the tensiometer, the surface tension of a distilled water droplet was measured. A glass syringe with an attached needle (stainless steel, 1.83 mm diameter) was inserted into the dosing system. Initially, the glass syringe was filled with distilled water and a glass slide was placed on the stand below the syringe. The syringe was lowered so that both the substrate and needle tip were in focus. The pendant drop mode was selected in the Drop Shape Analysis software, and the needle diameter was inputted into the drop information. Then the automatic dosing system was used to form a 30 μl drop. The surface tension of the distilled water droplet was measured to be 71 N/m which is in line with the literature value at room temperature [56].

The DSA software was switched to sessile droplet mode in order to measure the contact angles used in the analysis for this experiment. There are several methods of determining the contact angle: circle fit, conic section method, polynomial method and Young-Laplace fit. In this project, the droplets were low volume, approximately symmetrical and the contact angles ranged from 20° to 110° . This aligns with the optimal conditions to use the Young-Laplace fit method to calculate the contact angles [55].

The substrates were prepared as described in section 3.4. After placing a substrate on the stand beneath the syringe, the stand was raised so that the substrate was visible in the software image. A 2 μl droplet of colloidal dispersion was deposited directly below the needle, using a micro-pipette with the deposition technique outlined in section 3.2. The syringe was not used in order to maintain consistency in the deposition technique between the contact angle measurements and the microscopy. For each substrate, the initial contact angle was measured for three separate droplets and the mean was taken as the initial contact angle. Further measurements were taken for the contact angles and base diameters of the droplets over the duration of evaporation.

3.6 Bright-field microscopy

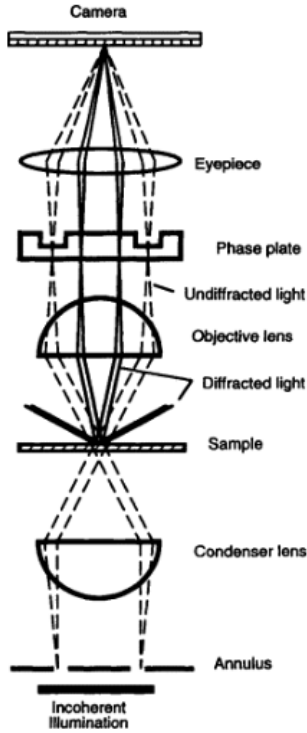


Figure 6. Schematic of the light path in a bright-field microscope [57].

Bright-field microscopy works by illuminating the sample from below, creating contrast where the specimen absorbs the transmitted light. Light travels from the source and is focused by the condenser lens onto the specimen which sits on the stage. The sample is imaged by the light passing through as the sample absorbs, scatters and deflects it. The light reaches the objective lens where it is directed to the eyepiece to be observed or recorded by a camera. This process is depicted in figure 6.

Bright-field microscopy is simple to perform and ideal for imaging the final deposits of the evaporating particle-laden droplets in this experiment. The particles that are deposited on the substrate will absorb the transmitted light and thus, in the images there are dark regions corresponding to the dried deposits on a bright background. However, bright-field microscopy is limited in that it is only suitable for individual particle tracking in ideal situations, and it cannot accurately image different height focal planes within a droplet during evaporation.

2 μ l droplets of the silica dispersion were deposited via micro-pipette onto the substrates and imaged with an upright microscope (Olympus Bx50) with a mounted camera (QICAM fast-cooled mono digital camera. 12-bit. QImaging) and objective (5x magnification, MUE12050, Nikon). Each sample was positioned using a stage connected to the microscope. The mono capture depth was set to 8-bit and the multi-image capture mode, sequence capture, was used to image each droplet during evaporation. The final deposits were imaged in single-capture mode.

For the untreated glass substrate, the deposit had to be captured in six shots due to its size. The FIJI Stitching plugin [58] was used to grid-stitch the images together. The result can be seen in figure 7. Several settings were utilised to minimise artefacts introduced from the stitching process: the overlap was set to 30%, regressions threshold 0.30, max/avg displacement threshold 2.5 and absolute displacement threshold 3.5. These were adjusted to minimise artefacts from the stitching, however, they were still present. To further reduce these artefacts, a background correction was applied. The *subtract background* process in FIJI was used to apply a rolling ball background subtraction to the image. This assigns a local background value to every pixel by averaging the intensity values over a given radius around each pixel. The local average values are subtracted from the original image pixel values to remove large spatial variations in the background intensities. A rolling ball radius of 60 pixels was determined to be the most effective at removing the artefacts while retaining the details of the original image. This background subtraction was applied to all the dried deposit images to maintain consistency between the images.

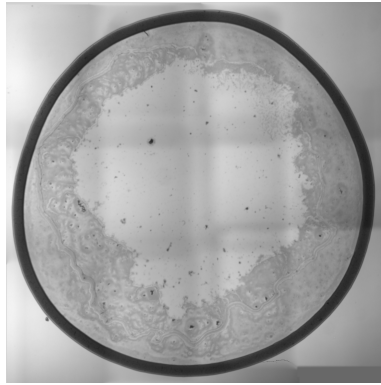


Figure 7. Dried deposit from the evaporation of a particle-laden droplet on untreated glass. Six images have been stitched together using the FIJI plugin grid stitch to form this image [58].

3.7 Characterising the Deposit

The images of the final deposits were stored in Python as 2D array grey-scale pixel intensities. All graphing was performed using the Python package Matplotlib [59]. The Python package, Skikit image [60], was used to take Hough transform circle fits of the images. This feature extraction technique was used to calculate the centres and radii of the final deposits. In particular, the *skimage.feature.canny* function which implements the Canny edge detection algorithm [61] to return a binary edge map was used first, taking the image arrays as its input as well as optional thresholding parameters for which the minimum threshold was set to 10, and the maximum threshold to 15. The detected edges were then passed to the *skimage.transform.hough_circle* function along with a range of estimated radii in units of pixels. This function returns an array of x, y, and radius values where x and y refer to the coordinates for the centre of each detected circle. The function, *skimage.transform.hough_circle_peaks*, takes the outputted parameters from

`skimage.transform.hough_circle` in addition to a ‘number of circles’ parameter n , from which it fits to the n most prominent circles in the image. The latter input, n , was set to 1 so that the function returned the centre coordinates and radius for the outermost perimeter of each dried deposit due to this outermost perimeter being the most prominent edge in all trials.

In this experiment, the ζ parameter was used to characterise the shapes of the deposits. For each deposit, an empty grid (a 2D array of zeros) was created in Python with each element corresponding to a pixel in the dried deposit image 2D array. The radial distance, r , from each point in the grid to the centre of the deposit, determined from the circle fit to the deposit edge, was calculated and the Numpy histogram function was used to bin the distances and return a count of the points in each bin, weighted by the corresponding image intensities, I . These weighted counts were first normalised by the number of points in their associated bin and then multiplied by the corresponding bin edges to give a single weighted image moment, ω , for each radial distance bin. The weighted image moment for the k^{th} bin is given by equation 18. These moments form the weighted profile of the image. From the weighted profile, the radial distance at the maximum weighted image moment has been extracted, r_ω^{max} , as well as the radial distance at the average weighted image moment, $\langle r_\omega \rangle$, defined in equation 19. The ratio of these values was used to characterise the dried deposits as described by equation 20, with a uniform ring giving $\zeta = 0.5$ and a perfect coffee ring giving $\zeta = 1$.

$$\omega_k = r_k I(r_k) \quad (18)$$

$$\langle r_\omega \rangle = \frac{\sum_i^N r_i I(r_i)}{\sum_i^N I(r_i)} \quad (19)$$

$$\zeta = \frac{\langle r_\omega \rangle}{r_\omega^{max}} \quad (20)$$

To test this parameter, ring-like deposit images were generated using Python and processed as outlined above, these are shown in figure 8. A 400x400 array was created with a zero-intensity background. Four parameters were defined: an inner radius, an outer radius and the minimum and maximum intensities. These parameters were used to produce two concentric circles with varying intensities between their radii to replicate dried deposits of varying intensity profiles. All the generated deposits had an outer radius of 150 pixels.

The first image (figure 8a) was generated with an inner radius of 140 pixels, and a uniform pixel intensity of 255. This represents what we have defined as a strong coffee ring; a thin, high-intensity ring with a low-intensity, uniform bulk. The ζ parameter for this image was $\zeta = 0.973$. The second image (figure 8b) was generated with an inner radius of 100 pixels and a pixel intensity range of 0 to 255. For this image, $\zeta = 0.895$. The third image (figure 8c) was generated with an inner radius of 0 pixels and pixel intensities ranging from 0 to 255, giving $\zeta = 0.673$. The last image (figure 8d) was generated with an inner radius of 0, and a uniform pixel intensity of 255, essentially resembling a uniform circular deposit. The ζ parameter for this image was $\zeta = 0.505$.

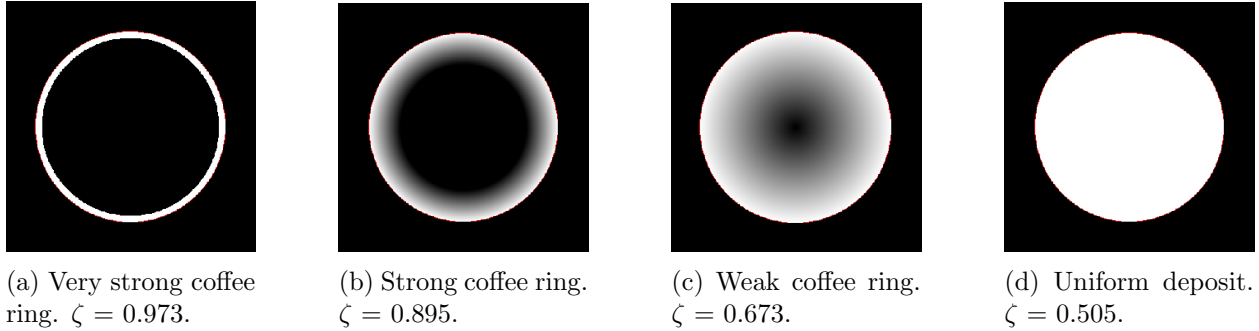


Figure 8. 150 pixel radius deposits on zero pixel intensity backgrounds generated using Python. The ζ parameters are displayed below each image.

3.8 Fluorescent microscopy

Fluorescent microscopy is a method that utilises the fluorescence of a specimen in order to image it in high resolution. There are several types of fluorescent microscopy: confocal microscopy, total internal reflection fluorescence microscopy, two-photon microscopy, structured illumination microscopy and superresolution microscopy. In this experiment, a confocal microscope was used because it is ideal for high-resolution 3D imaging. In confocal microscopy, focused beams of laser light are directed at a dichroic mirror which reflects the beams towards the objective lens. The lens focuses the laser onto a point in the sample in the desired focal plane. The fluorescent light emitted by the sample at that point travels through a pinhole aperture which blocks the out-of-focus light, such that only light from the desired focal plane reaches the detector. A single optical plane is imaged. By scanning several planes, the images can be stacked together to create a 3D visualisation of the sample [62]. A schematic for the confocal microscope is displayed in figure 9.

2 μl droplets of the fluorescent silica dispersion were deposited with a micro-pipette onto the substrates and imaged using a confocal microscope (Leica Microsystems, DMi8 TCS SP8) with an air objective (10x magnification, N Plan). The microscope scanned along the x and y axes at several different heights ranging over a vertical distance of 300 μm . Analysis has been performed at three heights within each droplet; near the base of the droplet, at a height $h = 19 \mu\text{m}$ above the surface, near the apex of the droplet, $h = 188 \mu\text{m}$, and at an intermediate height, $h = 113 \mu\text{m}$. These heights are only approximate since it was difficult to determine the exact positions of the substrate surfaces. The fluorescent silica particles were excited by a 488 nm laser and the emitted light was captured with a photomultiplier detector. The display format was 512 x 512 pixels, and the bit depth was 8 bits. A 2.5 zoom factor was selected and an 8000Hz scan frequency was used for all imaging resulting in a 2.17 second time interval between images on the same focal plane slice. The smart gain was set to 623.8, the smart offset to -0.0 and the beam intensity to 100% in the Leica settings for all measurements.

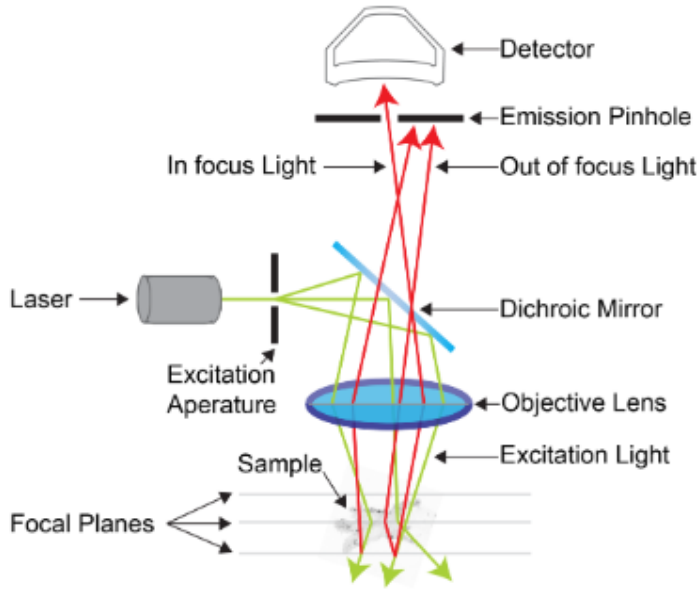


Figure 9. Schematic of a confocal microscope [63].

3.9 Particle tracking

The software FIJI, an image processing package distribution of ImageJ2, was used to track the particles imaged by the confocal microscope. In order to facilitate more accurate tracking, the contrast and brightness settings for the loaded frames were altered to lower the background pixel intensity and increase the particle pixel intensity. The display range was adjusted such that the minimum was 35 and the maximum was 38. The plugin Trackmate allowed for the automatic detection of the particles. In the import settings, the ‘View stack with’ setting was set to ‘Hyperstack’, and the option to ‘Specify range for each series’ was ticked. All other options were left on the default setting.

Once a hyperstack had been imported, the detector was selected. Several modes of particle detection were available in Trackmate including the Hessian detector, Difference of Gaussians (DoG) detector and Laplacian of Gaussian (LoG) detector which are all suited to spherical blob detection. The DoG detector is a feature detection algorithm software for single particle tracking. It identifies local maxima in the image that stand out from their surroundings by looking for the presence of high-intensity blobs in the image. The detector uses Gaussian filters of different standard deviations which involves convolving the image with Gaussian kernel matrices. It then subtracts different filtered images to create a difference of Gaussians image. The image will have a high intensity where the Gaussians differ the most. Thresholds are then used to extract the regions of high intensity which correspond to the particle locations. The Laplacian of Gaussian (LoG) detector is similar to the DoG detector. Gaussian filters are used to smooth the image before the Laplacian operator is applied, revealing regions with sharp changes in intensity. It uses this information to identify the local maxima and thus detect particle positions. The LoG detector demands more computational power

than the DoG detector but can be applied with high performance in situations with significant noise. The Hessian detector calculates the Hessian matrix of the Gaussian smoothed image. It provides information about the local intensity variations allowing for the features of the image to be identified. The eigenvalues of the Hessian matrix reveal the shape and size of the located features. The LoG detector was found to be optimal for detecting the silica colloidal particles in this experiment with reasonable computation time. It was used for droplet imaging for all three substrates.

The estimated object diameter was set to 10 μm and the quality threshold was set to 0. The quality threshold is an arbitrary measure of the likelihood that a detected spot will be relevant and it is useful for reducing the processing times when dealing with a large number of detected spots. In this experiment, performance issues with particle detection were not an issue so this initial quality threshold was not utilised. After object detection, initial thresholding was set to 0. These settings were selected so that the software overestimated the number of particles when performing object detection, allowing for all the visible particles to be included in the detection. The filter settings, ‘Std intensity ch1’ and ‘Contrast ch1’ were set to 5.14 and 0.11 respectively, to keep detected objects only where a particle was visible. This was done by observation and not every particle in each frame was detected. However, the large number of particles detected should represent the general movement of particles providing a broad understanding of the flow within the evaporating droplets. For tracking, the LAP tracker was selected. This tracker is based on the Linear Assignment Problem mathematical framework [64]. It first links the detected objects through consecutive frames, before searching for gap-closing, splitting and merging events. The default tracking parameters were used and frame-to-frame linking was set to 15 μm . The particle tracks were exported to CSV files to be analysed in Python.

The *Pandas* library [65] in Python was used to read the CSV files into data frames. Specifically, the frame number, time, and x and y position coordinates were converted to floats and stored as rows in a data frame. The ‘Track_ID’ numbers were also stored to indicate which rows corresponded to the same particle. From these values, the distance travelled by each particle in a given time period could be determined. The rows containing a unique track number were discarded since particles that had been recorded for a single frame were not useful for investigating particle movement. For each track number, the radial distance travelled between consecutive frames was calculated for every frame. The radial distance is defined as positive when a particle moves outward toward the contact line, and negative when moving towards the centre of the droplet. The centres of the droplets have been determined visually based on the images. The resolution of particle tracking with colloidal particles has been shown to be 1/10th of a pixel at best [66]. Hence, all recorded distances less than 0.08 μm between consecutive frames corresponding to a single particle were removed since these particles were considered stationary. For each frame, the distance travelled by every particle was summed to give a total distance travelled in the frame, which was then normalised by the number of particles present in the frame. This result was multiplied by the frames per second to give the average distance travelled per particle per second.

4 Results and Discussion

4.1 Dried deposits

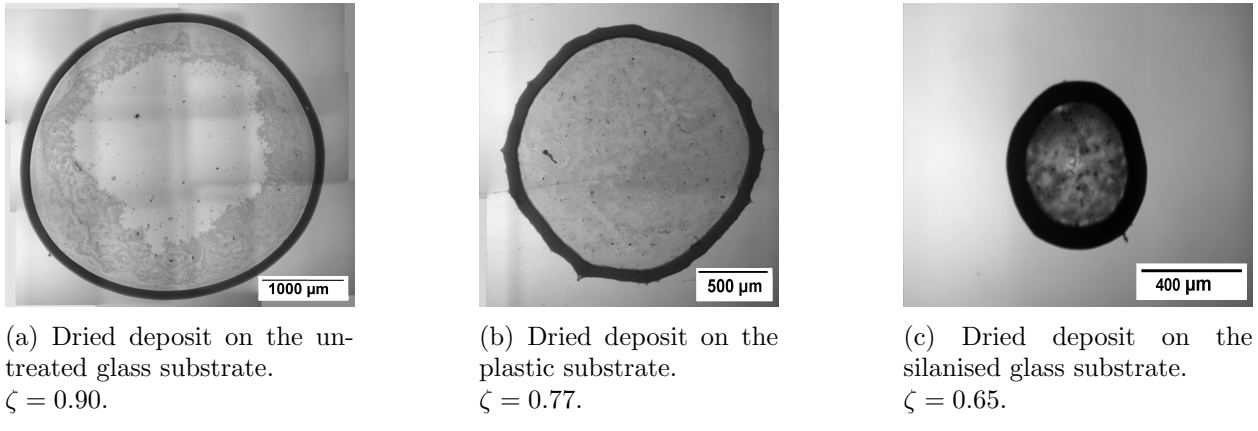
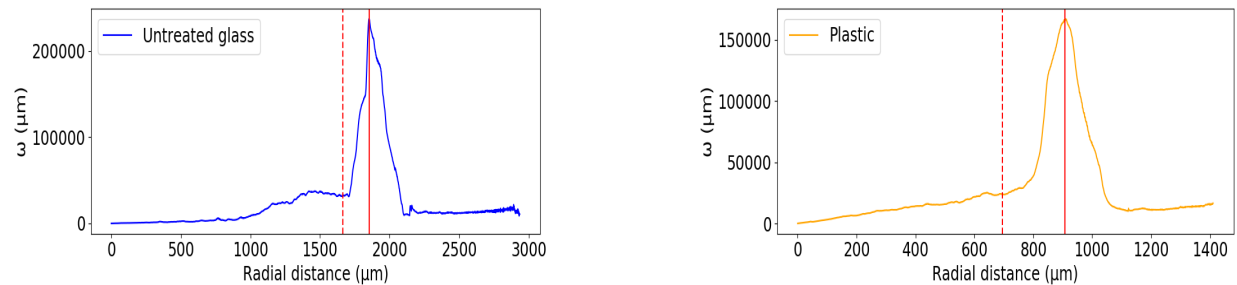
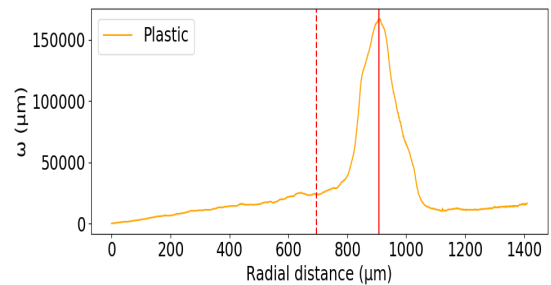


Figure 10. Bright-field images of dried deposits on the three different substrates.

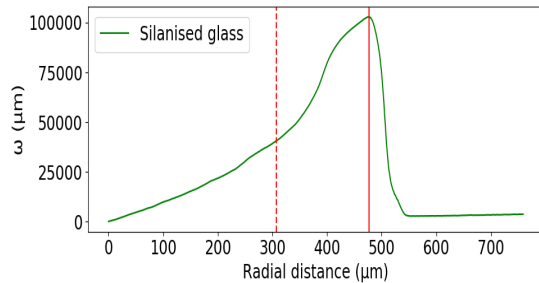
A coffee ring can be clearly observed for the untreated glass substrate deposit shown in figure 10a. There is a thin ring at the perimeter of the deposit, and on the inside of this ring, there is a slightly thicker non-uniform ring of higher pixel intensity. It should be noted here that higher intensity means less light absorbed by the sample, indicating fewer particles deposited in this region. Most of the bulk deposit, which we define as the area inside the deposit excluding the thin outer ring, is of a similar intensity to the background suggesting that very few particles have been deposited here. This agrees with the literature stating that for highly wettable substrates, contact line pinning results in outward particle flow near the base of the droplet and therefore a strong coffee ring is formed [14]. For the plastic substrate deposit shown in figure 10b, the coffee ring is still clearly observable, however, it is slightly thicker, relative to the radius of the deposit. It should also be noted that the edge of the deposit is more uneven, which is likely a result of the contact line depinning and subsequent deposition of particles at the droplet edge as it recedes. The web-like bulges suggest that perhaps the particles deposited at the droplet edge were resisting the receding of the contact line. This substantiates Deegan's theory that particles deposited at the droplet edge serve to pin the contact line [14]. Moreover, the bulk of this deposit contains darker regions throughout, suggesting that there was some particle deposition away from the contact line. This could be a result of the depinned contact line. For the silanised glass substrate deposit shown in 10c, again we see the web-like bulging at points along the contact line, indicating where the droplet has depinned. In this image, a low-intensity perimeter can still be observed and a coffee ring has formed, but in this case, the bulk is also significantly lower intensity than the background. This demonstrates that there has been significant particle deposition in the bulk of the droplet. Therefore, it appears that by increasing the initial contact angle of an evaporating sessile droplet one can expect an increasingly weak coffee ring. Finally, it is important to recognise that the radii of the deposits have also decreased with decreasing wettability (and increasing initial contact angle); the dried deposit



(a) Weighted profile for the dried deposit on the untreated glass substrate. $\zeta = 0.90$.



(b) Weighted profile for the dried deposit on the plastic substrate. $\zeta = 0.77$.



(c) Weighted profile for the dried deposit on the silanised glass substrate. $\zeta = 0.65$.

Figure 11. Plots of weighted image moments against radial distances from the deposits' centres for bright-field images of the dried deposits on the three different substrates. The solid red line indicates the radial distance at the maximum value of the weighted profile, r_ω^{max} , while the dashed red line indicates the image weighted average radius $\langle r_\omega \rangle$.

on the untreated glass substrate is much larger than the dried deposit on the silanised glass substrate. The relationship between the initial contact angles and ζ parameters, as well as corresponding errors, have been displayed in table 1. The mean values were calculated from three repeats on each of the substrates, and the displayed errors are the standard errors on these mean values. The random errors here are surprisingly small. We expect some error has been introduced by using Hough transform circle fits to determine the centres of the deposits which assume perfectly circular deposits. The deposits were roughly circular in shape but in some trials the deposits had rough edges or slight asymmetry which would have led to errors in these calculations. The small standard errors on the ζ parameters are reassuring because they suggest it was reasonable to assume symmetrical deposit shapes.

The weighted profile for each dried deposit image has been calculated from the pixel intensities and corresponding radial distances from the fitted circles' centres. It is important to note that for these weighted profile calculations, the pixel intensities in the dried deposit images (in figure 10) were flipped such that the dark rings represent maximum intensity while the backgrounds have minimum pixel intensities. An intensity-weighted bin count was carried out, and each bin was normalised by the number of particles in that radial bin such that each bin had an associated average pixel intensity. These average intensities were then multiplied by the upper bound radial distance of the associated bins to give an image moment and thus

Substrates	Mean CA_i ($^{\circ}$)	St.Err σ_{CA_i} ($^{\circ}$)	Mean ζ	St.Err σ_{ζ}
Glass	32.0	0.5	0.88	0.02
Plastic	46.6	0.5	0.75	0.01
Silglass	101.6	1.9	0.63	0.01

Table 1. The measured average initial contact angles and ζ parameters for each substrate. The averages were calculated from three trials for each substrate, and the errors quoted are the standard errors on these mean values.

the weighted profile. The weighted profiles have been plotted in figure 11. The solid red line indicates the radial distance at the maximum value of the weighted profile, r_{ω}^{max} , while the dashed red line indicates the image weighted average radius $\langle r_{\omega} \rangle$. The weighted profile for the silanised glass substrate deposit (figure 11c) is distinctly different from the other two plots. For the untreated glass substrate deposit, the image moments below $r = 1000$ μm are very small with only a slight positive gradient due to the image intensities at these radial distances being comparable to the background image intensities. At $r = 1000$ μm there is a sudden increase in gradient corresponding to the intermediate deposit between the thin outer coffee ring and the rest of the bulk deposit. At approximately $r = 1500$ μm , there is an even sharper gradient increase where we observe the spike corresponding to the main coffee ring. Compare this to the plastic deposit weighted profile (figure 11b) which has a significantly steeper uniform gradient increase from the centre of the droplet before a sharp increase at $r = 800$ μm corresponding to the inside edge of the coffee ring. In contrast, the weighted profile for the silanised glass deposit has no clear radial distance at which there is a significant increase in the image moment gradient, thus implying a significantly weaker outer ring. The strength of the coffee ring in each image has been defined by the ζ parameter discussed previously in section 3.1. The mean ζ parameters have been plotted against the initial contact angles in figure 12. There is clearly a downward trend showing that decreasing the initial contact angle decreases the strength of the coffee ring formation.

There are alternative methods to quantify the strength of a coffee ring such as the commonly used κ parameter. This is defined as:

$$\kappa = \frac{\bar{I}_{ring} - \bar{I}_{bulk}}{\bar{I}_{ring} - \bar{I}_{background}} \quad (21)$$

Where \bar{I}_{ring} is the average pixel intensity inside the ring, \bar{I}_{bulk} is the average pixel intensity inside the bulk of the deposit, and $\bar{I}_{background}$ is the average pixel intensity in the image background. For this approach, the image must be segmented into three distinct regions: the bulk, ring, and background. This is a complicated process that can cause issues when there are no clearly defined ring and bulk regions. When observing the dried deposit after evaporating a particle-laden droplet on the untreated glass surface, there is clearly a defined outer ring as well as a secondary ring of intermediate intensity which lies between the bulk and the outer ring. In such cases, it was difficult to determine what should qualify as the ring. By using the ζ parameter, no segmentation of the image was required, bypassing this issue entirely. Moreover, with the ζ parameter, both the radial distances and intensities are

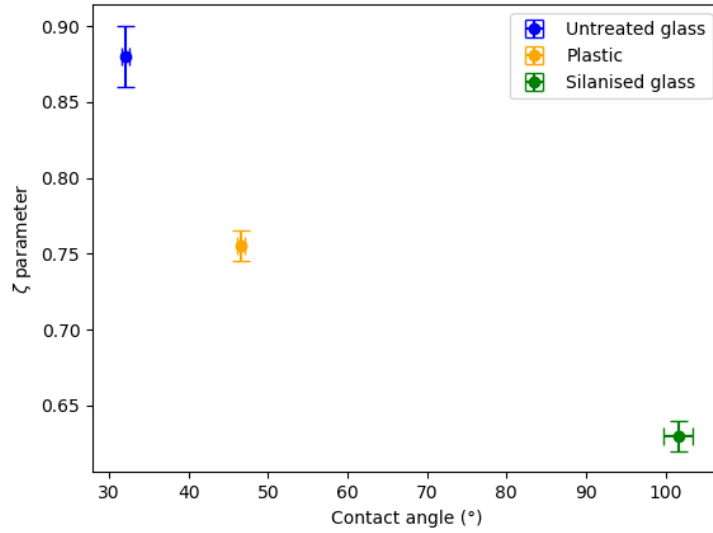


Figure 12. The mean ζ parameter against the mean initial contact angle, CA_i , for the three substrates.

taken into account, which means that in this system, a thin, defined ring with a large bulk radius is considered to be a stronger coffee ring than a much thicker ring with a smaller bulk radius. However, this can be problematic. Consider the two generated deposits below. The ring that fades from low intensity to high intensity (figure 13b) has a ζ parameter of 0.78 while the deposit with a clear discontinuity between the bulk and the ring (figure 13a) has a ζ parameter of 0.67. One might argue that the wider ring is a stronger coffee ring and thus using ζ here would be flawed. In such cases, it might be useful to introduce a secondary parameter proportional to the width of the dried deposit ring in order to fully characterise the deposit. In this experiment, this was not needed since particularly wide ring deposits were not encountered, but it should be a consideration for future work in this area.

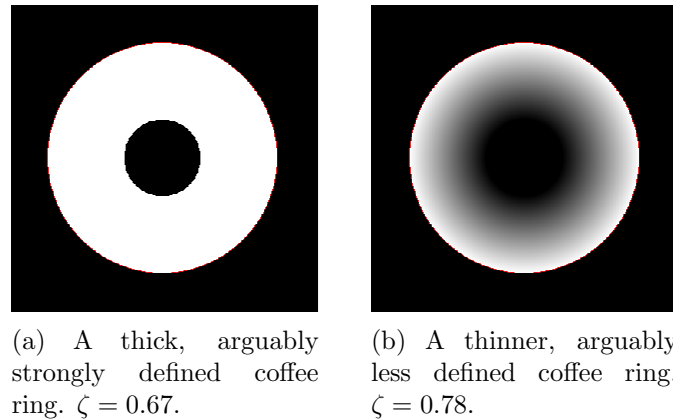


Figure 13. Images of deposits, generated using Python.

4.2 Drop shape analysis

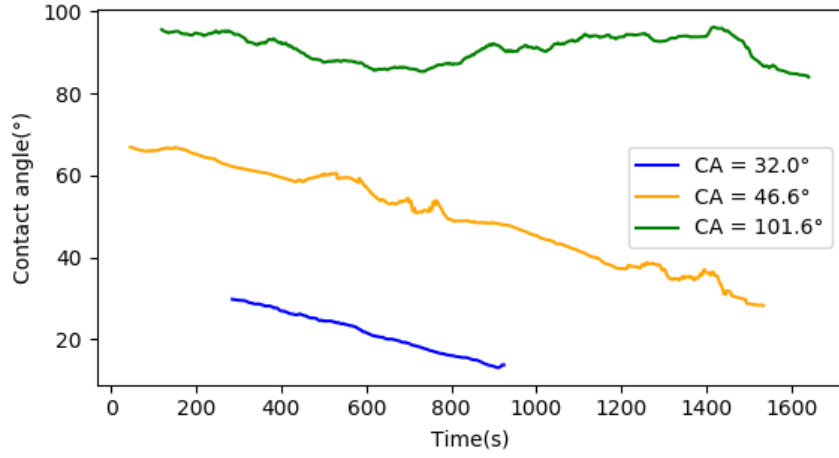
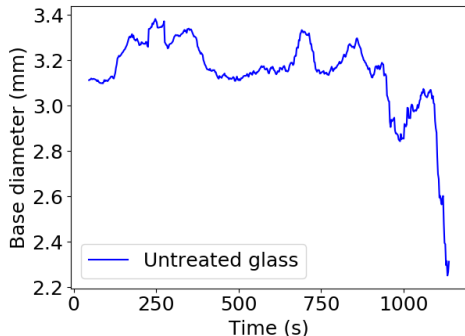


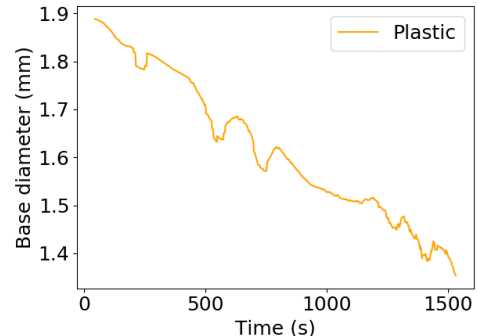
Figure 14. The droplet contact angles during evaporation on the three different substrates.

A Drop Shape Analyser was used in combination with a mounted Allied Vision Stingray camera to capture side-view imaging of the droplets during evaporation as described in section 3.1. The contact angles and base diameters of the droplets were recorded, and in this section, the results are discussed. It should be noted that data for the entire duration of evaporation has not been included. This is due to limitations in the experimental setup and fitting methods. Specifically, after significant evaporation, the droplets were too small in the images to be accurately fit using the DSA software. However, the contact angle and base diameter measurements could still provide useful information on the mode of evaporation (CCA or CCR) for each substrate. The contact angles of the droplets for the three different substrates have been plotted in figure 14 and base diameters in figure 15. It is clear that the initial base diameter of the droplet deposited on the untreated glass substrate (figure 15a) was significantly larger than the initial base diameters of the droplets on both the plastic substrate and silanised glass substrate. This is reassuring because for a more wettable surface, we would expect more spreading of the droplet and as a result, a higher base diameter. At initial contact angle $CA_i = 32.0^\circ$, the droplet had an approximately constant base diameter that slightly fluctuated around 3.2 mm until $t = 900$ s, when the base diameter dipped down to 2.8 mm. The base diameter slowly increased over the next 100s before dropping significantly. The small fluctuations around the initial base diameter imply CCR mode evaporation, indicating a pinned contact line. This is reinforced by the corresponding contact angle plot in figure 14, which displays a continually decreasing contact angle for the droplet evaporating on the untreated glass substrate. This is what we would expect from the literature; at low initial contact angles, contact line pinning causes CCR evaporation [14]. Furthermore, we conjecture that the smaller dip in base diameter, at $t = 900$ s, corresponds to depinning in late-stage evaporation resulting in the intermediate intensity inner ring observed in the bright-field image (figure 10a).

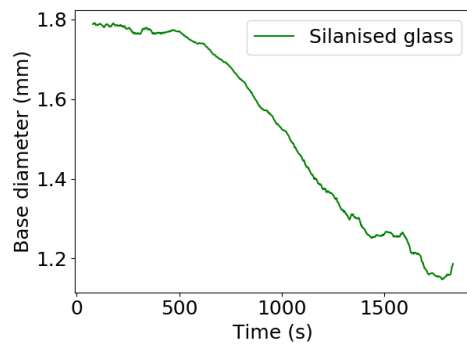
At $CA_i = 46.6^\circ$, the base diameter decreased from 1.9 mm to 1.4 mm throughout evaporation as shown in figure 15b. The decline is gradual and frequently levels off or even slightly in-



(a) Plot of base diameter against time for a droplet on the untreated glass substrate.



(b) Plot of base diameter against time for a droplet on the plastic substrate.



(c) Plot of base diameter against time for a droplet on the silanised glass substrate.

Figure 15. Plots of the base diameters of the droplets during evaporation on the three different substrates.

creases (for example at $t = 600\text{s}$). This implies that the droplet was predominantly depinned but frequently became pinned for periods of approximately one minute. The corresponding contact angle plot displays a similar gradual decline with frequent levelling off. This is somewhat surprising because it suggests that despite depinning and thus a receding contact line, the contact angle decreased simultaneously. Therefore, we observe a mixed mode of evaporation where there are no extended periods of CCA or CCR evaporation. At $CA_i = 101.6^\circ$, the initial base diameter was slightly below the initial base diameter for the droplet on the plastic substrate as shown in figure 15c. For this droplet we observed a near-constant base diameter until $t = 500\text{s}$, suggesting an initial pinning of the contact line. Over the next 800 seconds, the droplet was clearly depinned as the base diameter decreased at a constant rate. Moreover, this decrease occurred at a much faster rate than that of the droplet on the plastic substrate. The contact angle for this period of evaporation fluctuated around 90° . At approximately $t = 1300\text{s}$, the curve flattens out, before dipping and then flattening out again, throughout the duration of 500s. These events towards the final stages of evaporation suggest “stick-slip” behaviour, periods of contact line pinning and depinning in quick succession during evaporation, which has been observed in previous studies [67]. Sessile droplets on the untreated glass substrate and the silanised glass substrate have distinctly different evap-

oration processes, while evaporation on the plastic substrate has features similar to both; a decreasing base diameter in addition to a decreasing contact angle.

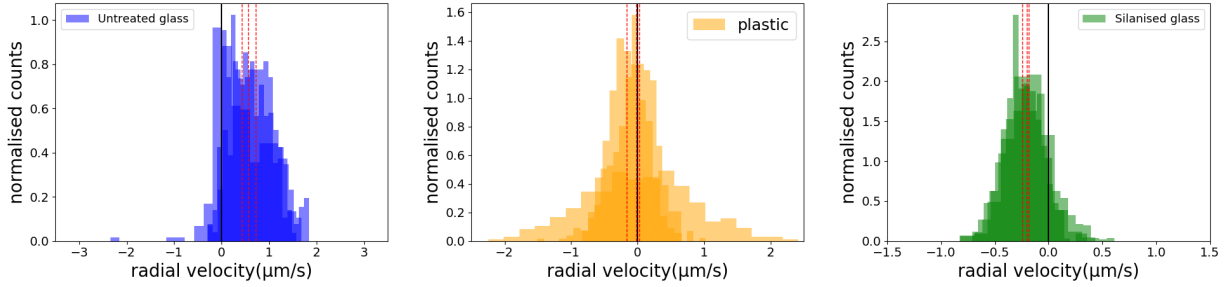
4.3 Flow of particles

The particle-laden sessile droplets were imaged with a confocal microscope, as described in section 3.1, to visualise the internal flows within the evaporating droplets. The centres of the droplets used to calculate radial distances in this analysis were determined manually by observation of the images and were treated as fixed points throughout the evaporation processes. We believed this to be a reasonable assumption since the three substrates were flat and smooth, so any contact line movement should have been symmetric about the centres of the droplets. Our previous bright-field sequence capture imaging supported this assumption. To quantitatively analyse the particle movement during droplet evaporation, the sum of the radial distances travelled by each detected particle was calculated for the three different substrates. In addition, the average distance travelled per particle per second was calculated by summing the distance travelled by each particle per frame to give a total distance travelled across each frame, and then normalising this by the number of particles present in the frame and multiplying by the frames per second.

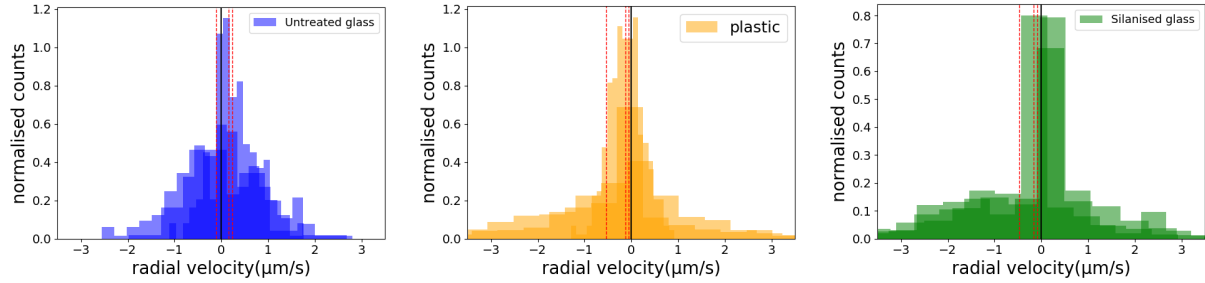
Normalised histograms for the particle velocities are displayed in figure 16. A black vertical line has been plotted at $\nu = 0 \mu\text{m/s}$ to separate inward radial flow (negative velocity) and outward radial flow (positive velocity), and the three red dashed lines represent the mean velocities of the three repeats taken for each substrate. At a height $h = 19 \mu\text{m}$ above the substrate surface, near the base of the droplet, the average radial velocity is positive (outward flow) for all three repeats performed on the untreated glass substrate. For both the plastic and silanised glass substrates, the average radial velocities are all negative, indicating inward flow at the base of the droplet. At $h = 113 \mu\text{m}$, the average radial velocity is positive for two out of the three repeats performed on the untreated glass substrate, and the average between the repeats is slightly positive. This suggests that there is less outward flow at this height in the droplet. Again the average radial velocities are negative for the plastic and silanised glass substrates. Finally, at $h = 188 \mu\text{m}$, an average velocity towards the centre of the droplet is observed for all three of the substrates. It should be noted that the inward flow velocity is significantly faster for the droplet evaporating on the untreated glass substrate.

To further investigate the average radial velocities, they have been plotted against height above the surface for the three different substrates in figure 17. This graph shows that the average particle velocities differ significantly at different heights within the droplet evaporating on the untreated glass substrate, whereas, for the plastic and silanised glass substrates, the average particle velocities do not vary as much with height. Moreover, despite having the largest outward flow near the base of the droplet, the droplet evaporating on the untreated glass substrate had a higher velocity inward flow at its apex than the droplets evaporating on the other substrates. The outward flow near the untreated glass surface aligns with the literature; for low contact angles, there is a predominant outward capillary flow which moves particles to the contact line [44]. This also supports our earlier findings that the droplet

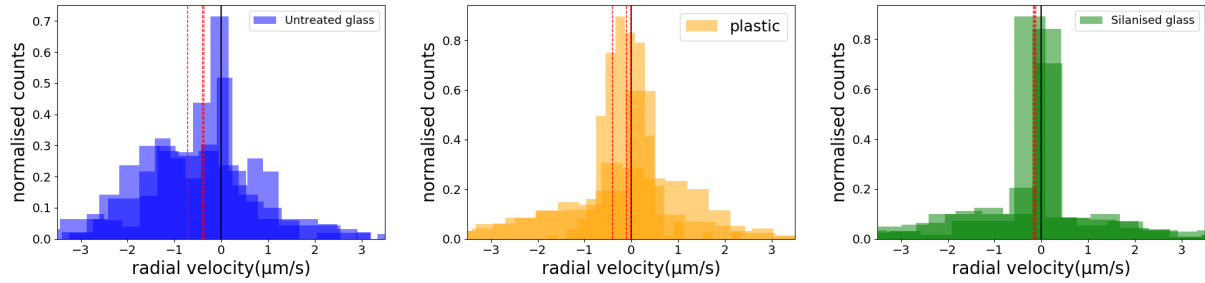
evaporating on the untreated glass substrate would leave a strong coffee ring characterised by a high ζ parameter, $\zeta = 0.88$. The large inward flows near the apex of the droplet, and very minor outward flows at an intermediate height support this view. The liquid lost at the base and near the centre of the droplet due to outward flows must be replenished, which we can infer flows down from the apex of the droplet. Therefore, we conjecture that the excess liquid at the contact line due to outward flow near the base of the droplet is balanced by inward flow at greater heights. A schematic for the average particle velocities within the droplet deposited on untreated glass is presented in figure 18a.



(a) Histograms of average particle velocity near the base of the droplet, $h = 19 \mu\text{m}$. Left: Untreated glass substrate. Middle: Plastic substrate. Right: Silanised glass substrate.



(b) Histograms of average particle velocity at $h = 113 \mu\text{m}$. Left: Untreated glass substrate. Middle: Plastic substrate. Right: Silanised glass substrate.



(c) Histograms of average particle velocity at $h = 188 \mu\text{m}$. Left: Untreated glass substrate. Middle: Plastic substrate. Right: Silanised glass substrate.

Figure 16. Histograms for average particle velocities at different heights within the droplets on the three different substrates. The three repeats at each height for each substrate are displayed by the three different opacities in each plot. The solid black line marks $\nu = 0 \mu\text{m/s}$ and the three red dashed lines represent the mean velocities of the three repeats.

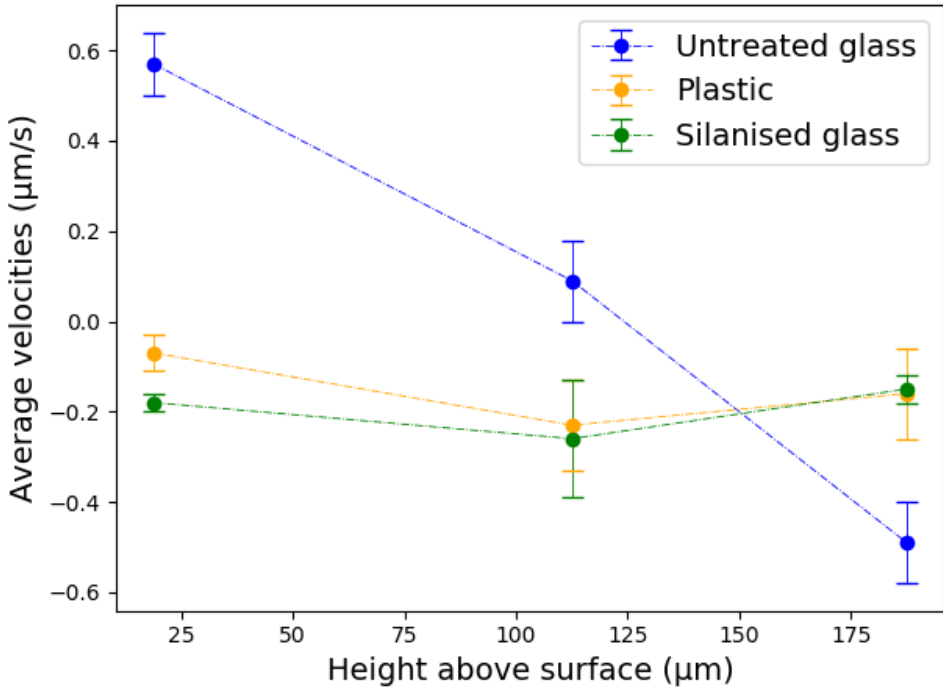


Figure 17. Average particle velocity against height within a droplet for droplets deposited on the three different substrates.

We observe inward flow at similar radial velocities at both $h = 113 \mu\text{m}$ and $h = 188 \mu\text{m}$ for the silanised glass and plastic substrates. When considering the uncertainties on these measurements, there is no difference between the radial velocities at these heights, despite a large difference in initial contact angle, $\Delta CA_i = 57.6^\circ$. At the base of the droplets, we also observe inward flows, but these are of higher velocity for the droplet on the silanised glass substrate. The dried deposits remaining after evaporation are visibly very different. The silanised glass substrate dried deposit is significantly more uniform and, as such, has a lower ζ parameter of $\zeta = 0.63$ than the plastic substrate dried deposit, with $\zeta = 0.75$. Schematics for the average particle velocities within the droplets deposited on the plastic and silanised glass substrates are presented in figures 18b and 18c.

We speculated that the inward flow observed in the plastic and silanised glass substrate cases could be a symptom of the depinned contact line; the inward movement of the contact line pushing the particles towards the centre of the droplet. To investigate this, ImageJ particle tracking was performed with additional filters utilised to isolate the particles at the contact line, thus allowing for the measurement of the velocity of the contact line which is shown in figure 19. Specifically, the contrast filters and minimum intensity filters were adjusted since there was generally higher intensity and less contrast due to the build-up of particles at the contact line. By plotting the difference between the average velocity of particles at the contact line, ν_{CL} , and the average velocity of particles in the entire droplet, ν , (figure 20) the origins of the inward flow could be investigated. For the glass substrate, where there was no observed contact line depinning, the measured particle velocity at the contact line

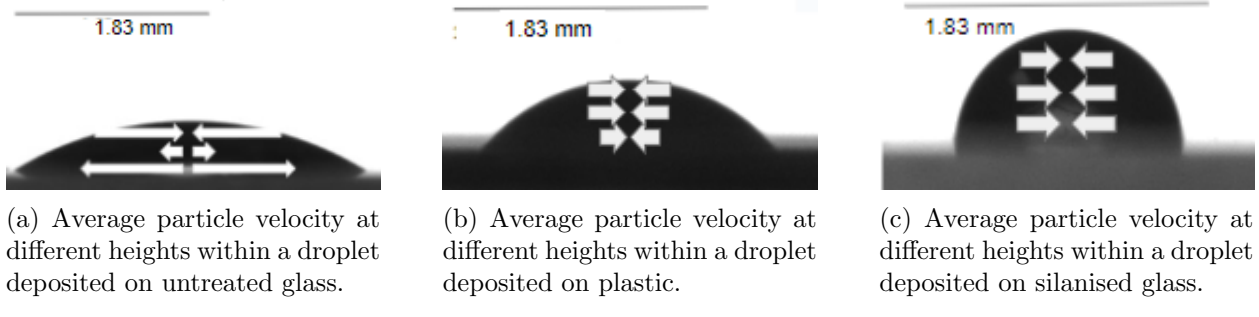


Figure 18. Side-view schematics displaying internal flows within the droplets based on the average velocities at different heights.

was $0.025 \mu\text{m}/\text{s}$, so this was considered to be the error on the contact line velocities. The graphs demonstrate a faster inward movement of the contact line for the droplet on the silanised glass substrate compared to the droplet on the plastic substrate. Interestingly, for the plastic substrate, the difference between the edge velocity and average particle velocity is approximately zero, which supports the hypothesis that the inward flow is driven by the moving contact line. For the silanised glass substrate, the difference is slightly greater than zero, implying that the velocity with which the contact line recedes is slightly greater than the average inward velocity of the particles in the droplet. These results should be interpreted with the understanding that the filtering used to track edge particles was done by observation and thus the errors may have been underestimated here.

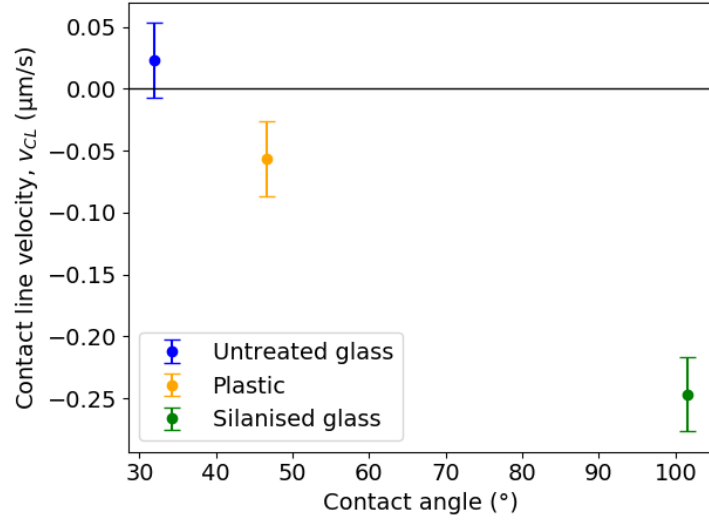


Figure 19. Plot of average particle velocity at the droplet contact line, v_{CL} , at the base of the droplet for the three different substrates. The velocity values are taken to be the averages of the three repeats for each substrate.

In addition to investigating the average velocity for the duration of evaporation, it is useful

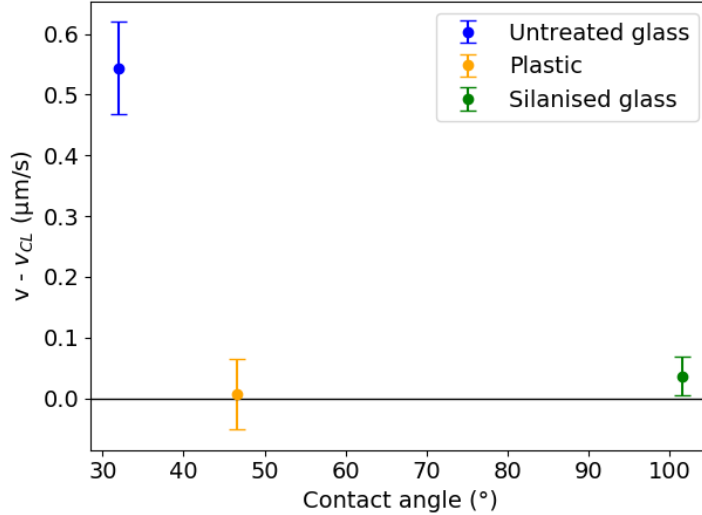


Figure 20. Plot of the difference between average particle velocity within the droplet and average particle velocity at the contact line at the base of the droplet. The results for all three substrates have been displayed. The velocity values are the averages of the three repeats for each substrate.

to observe how the motion of particles evolves with time. The radial distance travelled between each frame has been calculated for each particle and averaged to give a total radial distance travelled per frame. In order to improve the clarity of these results and show the trends in the data, the Numpy function, *np.convolve*, has been used to perform a smoothing convolution between the radial distances and a given kernel. A 21-point unweighted filter was used to convolve the data, resulting in smooth curves without losing the important features of the raw data. This kernel size was selected by trial and error calculations to smooth the data enough to visualise trends while still retaining the plots' features. The results have been plotted against time as shown in figure 22. Contact angles plots have been included in figure 22a for reference. It should be noted that the contact angle measurements were recorded over the duration of evaporation for each droplet, whereas the confocal imaging has not captured the early stages of evaporation. For the untreated glass substrate, $CA_i = 32.0^\circ$, at $h = 19 \mu\text{m}$, we observe an initial outward movement at a low average particle velocity of approximately $0.3 \mu\text{m/s}$. After 100 seconds, an increasingly fast outward movement occurs, reaching a peak of $1.2 \mu\text{m/s}$ at $t = 300\text{s}$. There is then a sharp decrease in velocity down to $0 \mu\text{m/s}$ suggesting that most of the particles at this stage are stationary and likely deposited. The increasingly fast outward radial movement is likely a phenomenon described by A.G Marin et al. as “rush-hour” for particles in an evaporating colloidal droplet [68] which is a rapid movement of particles to the contact line near the end of the evaporation process.

At $h = 113 \mu\text{m}$, there are three separate peaks in average velocity. In the first 2200 seconds of evaporation, there are two smaller peaks reaching $0.3 \mu\text{m/s}$, before a large peak to $0.7 \mu\text{m/s}$ at approximately $t = 300\text{s}$. At $h = 188 \mu\text{m}$, the flow is directed inwards. Note that the shorter time frame is due to the height of the droplet decreasing during evaporation such that the apex of the droplet falls below the height of the focal plane. The inward flows are

reassuring because it appears that these flows are the source of replenishing the lost liquid at the centre of the droplet due to the predominant outward flow at the base of the droplet. This is displayed in figure 21. These inward flows likely arise from surface tension effects induced by a temperature gradient along the free surface of the droplet that could be due to higher evaporation flux at the droplet edge. Other sources of Marangoni flow may also be in effect here, such as the difference in thermal conductivity between the solid substrate and liquid droplet, inducing vertical temperature gradients.

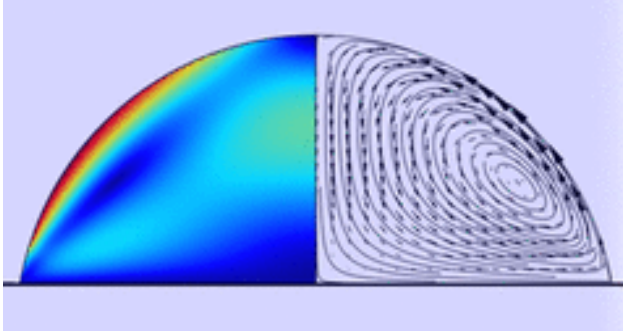
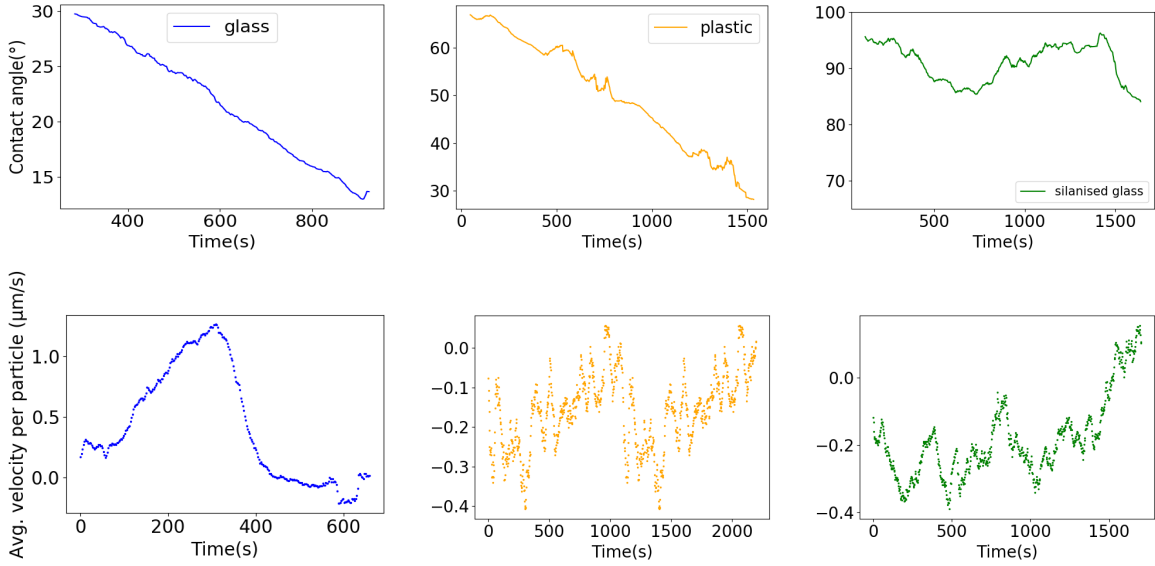
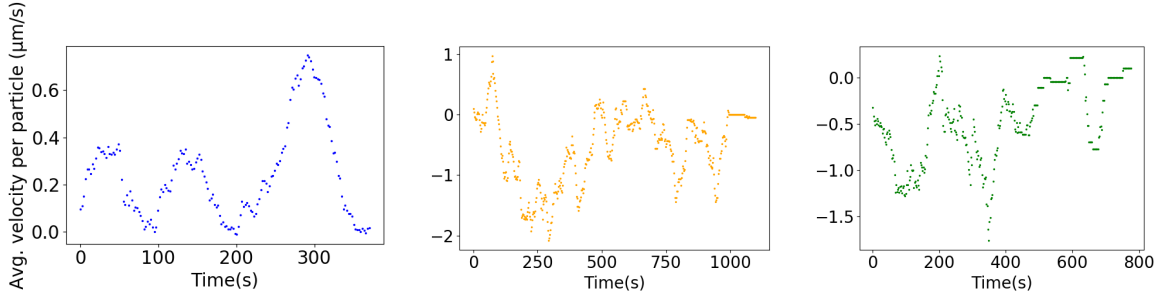


Figure 21. Schematic of flows within a droplet evaporating on a substrate with low initial contact angle. There are outward radial flows at the base of the droplet and inward radial flows near the apex of the droplet [69].

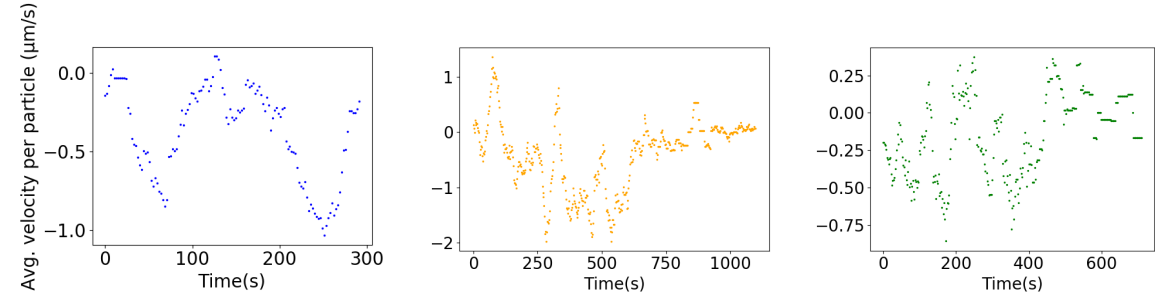
For the plastic substrate, $CA_i = 46.6^\circ$, at $h = 19 \mu\text{m}$ the average velocity is initially negative indicating inward flow, but throughout evaporation, this seems to oscillate around an average velocity of approximately $-0.1 \mu\text{m/s}$, with troughs reaching approximately $|\nu| = 0.3 \mu\text{m/s}$. In fact, we observe a similar shape for the plots at $h = 113 \mu\text{m}$ and $h = 188 \mu\text{m}$ as well. Indicating periods of both outward and inward flow at all heights in the droplet. This aligns with results from the side-view imaging, which revealed mixed modes of evaporation for the droplet on the plastic substrate. Moreover, the defined coffee ring as well as particles deposited in the bulk revealed via the bright-field images suggest that this mixture of modes has led to a deposit that appears intermediate between the higher and lower CA_i deposits. The average velocity plots for evaporation on the silanised glass substrate show almost exclusively inward flows near the base of the droplet for the entire duration. It is important to note that the magnitude of average radial velocity does not exceed $0.5 \mu\text{m/s}$ which is significantly slower than the average outward velocity near the base of the untreated glass substrate. Furthermore, the average velocity fluctuates around $-0.3 \mu\text{m/s}$ for approximately 800s, which demonstrates more of a constant inward flow compared to the outward rush observed in the untreated glass substrate case. This provides further evidence to support the earlier claims that the inward flows were largely due to the receding edge of the droplet pushing the particles towards the centre. Evaporation in the CCA mode demands a receding contact line and thus replenishing flows to the edge of the droplet driven by capillary action are not required [14].



(a) Top: Contact angles of the evaporating sessile drops on each substrate. Bottom: Average particle velocity against time at a height above the surface $h = 19\mu\text{m}$. Left: Glass substrate. Centre: Plastic substrate. Right: Silanised glass substrate.



(b) Average particle velocity against time at a height above the surface $h = 113\mu\text{m}$. Left: Glass substrate. Centre: Plastic substrate. Right: Silanised glass substrate.



(c) Average particle velocity against time at a height above the surface $h = 188\mu\text{m}$. Left: Glass substrate. Centre: Plastic substrate. Right: Silanised glass substrate.

Figure 22. Plots of average particle velocity against time at different heights within a droplet for the three different substrates. In (a), contact angle plots have been included for comparison.

5 Conclusion

In this project, the effects of surface wettability on the internal flows within evaporating sessile droplets and the resultant dried deposits have been investigated. From the experiments carried out it is clear that the initial contact angle between an evaporating sessile droplet and a substrate significantly affects the evaporation process. The outward flows for low initial contact angle and inward flows for high initial contact angle evaporation observed near the base of the droplet align with what is outlined in the preprint on surface wettability and evaporation processes by C.M Perez et al. [20]. In addition, we observed a strong coffee ring on the untreated glass, a high wettability substrate, and a significantly less clear ring with clear signs of depinning for droplet evaporation on silanised glass. These deposit patterns also agree with the observations made in the preprint. In this project, we aimed to investigate the evaporative flows at different heights within the droplet. Our results showed large inward flows near the apex of the droplet evaporating on untreated glass, and small inward flows throughout the droplets evaporating on plastic and silanised glass substrates.

The side-view, bright-field and confocal imaging were all useful in understanding the evaporative flows inside a particle-laden sessile droplet. The side-view analysis showed that at a low initial contact angle, the evaporation occurred primarily in the CCR mode, implying contact line pinning. The bright-field images revealed a strong coffee ring formation on the untreated glass substrate, with $\zeta = 0.88$. This aligns with Deegan's assertion that for low contact angles, outward capillary flows cause contact line pinning leading to particle deposition at the contact line [14]. We observed further evidence for this in the confocal measurements; a rush of particles out towards the contact line. For high initial contact angle, $CA_i = 104.2^\circ$, the side-view analysis revealed that the CCA mode was the predominant mode of evaporation. This is indicative of contact line depinning. The dried deposit was determined to have $\zeta = 0.63$ from the bright-field image analysis, a deposit that is significantly more uniform than the deposits left on the untreated glass and plastic substrates. The confocal images offered an explanation for these results as we see no outward flows near the base of the droplet but rather, slight inward flows throughout the droplet. Further particle tracking analysis demonstrated a similar average particle velocity to the contact line velocity which could suggest that the movement of particles towards the centre of the droplet was predominantly due to the receding edge of the droplet pushing the particles inwards. For the intermediate initial contact angle, $CA_i = 46.6^\circ$, we observed that there was a mixture of modes during evaporation, both the contact angle and the base diameter of the droplet were, in general, decreasing. Imaging from the bright-field microscope revealed the formation of a thicker coffee ring relative to the deposit radius compared to the deposit left on the untreated glass substrate, in addition to a lower intensity bulk suggesting particle deposition in the bulk of the deposit. A clear coffee ring forms despite determining from the confocal imaging that the average velocity of the particles near the base of the droplet was slightly negative, meaning inward flow. However, when measuring the average particle velocity over time, we found oscillations around zero, suggesting periods of outward flow which are likely the source of the coffee ring formation.

These results imply that the strength of the coffee ring formation changes gradually with the initial contact angle, rather than a shift from a strong coffee ring to a uniform deposit based

purely on whether the contact line depins. Overall, the relationship between wettability and the strength of a ring-like stain deposit has been explored extensively in this project. The image analysis of silica particle-laden droplets deposited on three substrates of varying initial contact angles has given results near the base of the droplets that are in agreement with C.M. Perez's work in the preprint [20]. Furthermore, the image analysis at different heights within the droplets has provided additional insights into the evaporative flows of sessile droplets.

References

- [1] Jungho Park and Jooho Moon. Control of colloidal particle deposit patterns within picoliter droplets ejected by ink-jet printing. *Langmuir*, 22(8):3506–3513, 2006.
- [2] Andreas Friederich, Joachim R Binder, and W Bauer. Rheological control of the coffee stain effect for inkjet printing of ceramics. *Journal of the American Ceramic Society*, 96(7):2093–2099, 2013.
- [3] Minxuan Kuang, Libin Wang, and Yanlin Song. Controllable printing droplets for high-resolution patterns. *Advanced materials*, 26(40):6950–6958, 2014.
- [4] Jungho Park, Jooho Moon, Hyunjung Shin, Dake Wang, and Minseo Park. Direct-write fabrication of colloidal photonic crystal microarrays by ink-jet printing. *Journal of colloid and interface science*, 298(2):713–719, 2006.
- [5] Liying Cui, Yingfeng Li, Jingxia Wang, Entao Tian, Xingye Zhang, Youzhuan Zhang, Yanlin Song, and Lei Jiang. Fabrication of large-area patterned photonic crystals by ink-jet printing. *Journal of Materials Chemistry*, 19(31):5499–5502, 2009.
- [6] Jiao-Jing Shao, Wei Lv, and Quan-Hong Yang. Self-assembly of graphene oxide at interfaces. *Advanced Materials*, 26(32):5586–5612, 2014.
- [7] Jianli Zou and Franklin Kim. Diffusion driven layer-by-layer assembly of graphene oxide nanosheets into porous three-dimensional macrostructures. *Nature communications*, 5(1):5254, 2014.
- [8] Ralf Blossey and Andreas Bosio. Contact line deposits on dna microarrays: a “twin-spot effect”. *Langmuir*, 18(7):2952–2954, 2002.
- [9] Vincent Dugas, Jérôme Broutin, and Eliane Souteyrand. Droplet evaporation study applied to dna chip manufacturing. *Langmuir*, 21(20):9130–9136, 2005.
- [10] Weiping Zhou, Anming Hu, Shi Bai, Ying Ma, and Quanshuang Su. Surface-enhanced raman spectra of medicines with large-scale self-assembled silver nanoparticle films based on the modified coffee ring effect. *Nanoscale research letters*, 9:1–9, 2014.
- [11] Weidong Wang, Yongguang Yin, Zhiqiang Tan, and Jingfu Liu. Coffee-ring effect-based simultaneous sers substrate fabrication and analyte enrichment for trace analysis. *Nanoscale*, 6(16):9588–9593, 2014.
- [12] Yin-Hung Lai, Yi-Hong Cai, Hsun Lee, Yu-Meng Ou, Chih-Hao Hsiao, Chien-Wei Tsao, Huan-Tsung Chang, and Yi-Sheng Wang. Reducing spatial heterogeneity of maldi samples with marangoni flows during sample preparation. *Journal of The American Society for Mass Spectrometry*, 27(8):1314–1321, 2016.
- [13] Olena Kudina, Burak Eral, and Frieder Mugele. e-maldi: an electrowetting-enhanced drop drying method for maldi mass spectrometry. *Analytical chemistry*, 88(9):4669–4675, 2016.

- [14] Robert D Deegan, Olgica Bakajin, Todd F Dupont, Greb Huber, Sidney R Nagel, and Thomas A Witten. Capillary flow as the cause of ring stains from dried liquid drops. *Nature*, 389(6653):827–829, 1997.
- [15] Shyamashis Das, Atreya Dey, Govardhan Reddy, and DD Sarma. Suppression of the coffee-ring effect and evaporation-driven disorder to order transition in colloidal droplets. *The journal of physical chemistry letters*, 8(19):4704–4709, 2017.
- [16] Peter J Yunker, Tim Still, Matthew A Lohr, and AG Yodh. Suppression of the coffee-ring effect by shape-dependent capillary interactions. *nature*, 476(7360):308–311, 2011.
- [17] Lalit Bansal, Pranjal Seth, Bhubesh Murugappan, and Saptarshi Basu. Suppression of coffee ring:(particle) size matters. *Applied Physics Letters*, 112(21):211605, 2018.
- [18] A Crivoi and Fei Duan. Amplifying and attenuating the coffee-ring effect in drying sessile nanofluid droplets. *Physical Review E*, 87(4):042303, 2013.
- [19] Hua Hu and Ronald G Larson. Marangoni effect reverses coffee-ring depositions. *The Journal of Physical Chemistry B*, 110(14):7090–7094, 2006.
- [20] Carmen Morcillo Perez, Marcel Rey, Benjamin D Goddard, and Job HJ Thijssen. Changing the flow profile and resulting drying pattern of dispersion droplets via contact angle modification. *arXiv preprint arXiv:2111.00464*, 2021.
- [21] Sumesh P Thampi and Madivala G Basavaraj. Beyond coffee rings: Drying drops of colloidal dispersions on inclined substrates. *ACS omega*, 5(20):11262–11270, 2020.
- [22] RG Picknett and R Bexon. The evaporation of sessile or pendant drops in still air. *Journal of colloid and Interface Science*, 61(2):336–350, 1977.
- [23] Hanneke Gelderblom, Christian Diddens, and Alvaro Marin. Evaporation-driven liquid flow in sessile droplets. *Soft matter*, 2022.
- [24] Nagesh D Patil, Prathamesh G Bange, Rajneesh Bhardwaj, and Atul Sharma. Effects of substrate heating and wettability on evaporation dynamics and deposition patterns for a sessile water droplet containing colloidal particles. *Langmuir*, 32(45):11958–11972, 2016.
- [25] Peter J Lu and David A Weitz. Colloidal particles: crystals, glasses, and gels. *Annu. Rev. Condens. Matter Phys.*, 4(1):217–233, 2013.
- [26] Jean Perrin. *Brownian movement and molecular reality*. Courier Corporation, 2013.
- [27] Jinjiang Li, Yuan Cheng, Xiaodong Chen, and Songyan Zheng. Impact of electroviscous effect on viscosity in developing highly concentrated protein formulations: lessons from non-protein charged colloids. *International Journal of Pharmaceutics: X*, 1:100002, 2019.
- [28] Gregory S Tschumper. Computations for weak noncovalent. *Rev. Comput. Chem*, 26:39, 2008.

- [29] Kristel Goovaerts, Paul Lambrechts, Jan De Munck, Lars Bergmans, and Bart Van Meerbeek. *Encyclopedia of materials: science and technology*. Elsevier Science, 2002.
- [30] Hari Singh Nalwa. *Handbook of surfaces and interfaces of materials, five-volume set*. Elsevier, 2001.
- [31] Rizwan Muneer, M Rehan Hashmet, and Peyman Pourafshary. Fine migration control in sandstones: Surface force analysis and application of dlvo theory. *ACS omega*, 5(49):31624–31639, 2020.
- [32] Susan A. Barker. Suspensions. <https://basicmedicalkey.com/suspensions/>, March 18, 2023. [Online; accessed 19-February-2023].
- [33] David E Alexander. *Nature's Machines: An Introduction to Organismal Biomechanics*. Academic Press, 2017.
- [34] George Gabriel Stokes. On the effect of the internal friction of fluids on the motion of pendulums. *Cambridge Library Collection - Mathematics*, 11(2):1—10, 1851.
- [35] Eli Ruckenstein and Dennis C Prieve. Dynamics of cell deposition on surfaces. *Journal of Theoretical Biology*, 51(2):429–438, 1975.
- [36] A Marmur, WN Gill, and E Ruckenstein. Kinetics of cell deposition under the action of an external field. *Bulletin of Mathematical Biology*, 38:713–721, 1976.
- [37] Eleni Dokou, Mark A Barteau, Norman J Wagner, and Abraham M Lenhoff. Effect of gravity on colloidal deposition studied by atomic force microscopy. *Journal of colloid and interface science*, 240(1):9–16, 2001.
- [38] Robert Brown. Xxvii. a brief account of microscopical observations made in the months of june, july and august 1827, on the particles contained in the pollen of plants; and on the general existence of active molecules in organic and inorganic bodies. *The philosophical magazine*, 4(21):161–173, 1828.
- [39] Albert Einstein. Über die von der molekularkinetischen theorie der wärme geforderte bewegung von in ruhenden flüssigkeiten suspendierten teilchen. *Annalen der physik*, 4, 1905.
- [40] Albert Einstein. *Investigations on the Theory of the Brownian Movement*. Courier Corporation, 1956.
- [41] Dennis C Prieve and Eli Ruckenstein. Effect of london forces upon the rate of deposition of brownian particles. *AICHE Journal*, 20(6):1178–1187, 1974.
- [42] HB Eral, DJCM t Mannetje, and Jung Min Oh. Contact angle hysteresis: a review of fundamentals and applications. *Colloid and polymer science*, 291(2):247–260, 2013.
- [43] Hua Hu and Ronald G Larson. Evaporation of a sessile droplet on a substrate. *The Journal of Physical Chemistry B*, 106(6):1334–1344, 2002.

- [44] Duyang Zang, Sujata Tarafdar, Yuri Yu Tarasevich, Moutushi Dutta Choudhury, and Tapati Dutta. Evaporation of a droplet: From physics to applications. *Physics Reports*, 804:1–56, 2019.
- [45] David Andrews, Thomas Nann, and Robert H Lipson. *Comprehensive nanoscience and nanotechnology*. Academic press, 2019.
- [46] Hua Hu and Ronald G Larson. Analysis of the effects of marangoni stresses on the microflow in an evaporating sessile droplet. *Langmuir*, 21(9):3972–3980, 2005.
- [47] John J Hegseth, N Rashidnia, and A Chai. Natural convection in droplet evaporation. *Physical review E*, 54(2):1640, 1996.
- [48] Annie Steinchen and Khellil Sefiane. Self-organised marangoni motion at evaporating drops or in capillary menisci—thermohydrodynamical model. *Journal of Non-Equilibrium Thermodynamics*, 30(1):39–51, 2005.
- [49] Cosimo Buffone and Khellil Sefiane. Investigation of thermocapillary convective patterns and their role in the enhancement of evaporation from pores. *International Journal of Multiphase Flow*, 30(9):1071–1091, 2004.
- [50] Olivier Raccourt, Jean Berthier, Philippe Clementz, Mathias Borella, and Marc Plissonnier. On the influence of surfactants in electrowetting systems. *Journal of Micromechanics and Microengineering*, 17(11):2217, 2007.
- [51] Pavlo Takhistov and Hsueh-Chia Chang. Complex stain morphologies. *Industrial & engineering chemistry research*, 41(25):6256–6269, 2002.
- [52] Douglas J Durian and Carl Franck. Continued exploration of the wetting phase diagram. *Physical Review B*, 36(13):7307, 1987.
- [53] Thomas Young. Iii. an essay on the cohesion of fluids. *Philosophical transactions of the royal society of London*, 95(3):65–87, 1805.
- [54] Daniel Bonn, Jens Eggers, Joseph Indekeu, Jacques Meunier, and Etienne Rolley. Wetting and spreading. *Reviews of modern physics*, 81(2):739, 2009.
- [55] Krüss. Drop shape analysis. <https://www.kruss-scientific.com/en/know-how/glossary/drop-shape-analysis>, December 1, 2017. [Online; accessed 11-February-2023].
- [56] NB Vargaftik, BN Volkov, and LD Voljak. International tables of the surface tension of water. *Journal of Physical and Chemical Reference Data*, 12(3):817–820, 1983.
- [57] Gordon S Kino and Timothy R Corle. *Confocal scanning optical microscopy and related imaging systems*. Academic Press, 1996.
- [58] Stephan Preibisch, Stephan Saalfeld, and Pavel Tomancak. Globally optimal stitching of tiled 3d microscopic image acquisitions. *Bioinformatics*, 25(11):1463–1465, 2009.

- [59] J. D. Hunter. Matplotlib: A 2d graphics environment. *Computing in Science & Engineering*, 9(3):90–95, 2007.
- [60] Stefan Van der Walt, Johannes L Schönberger, Juan Nunez-Iglesias, François Boulogne, Joshua D Warner, Neil Yager, Emmanuelle Gouillart, and Tony Yu. scikit-image: image processing in python. *PeerJ*, 2:e453, 2014.
- [61] John Canny. A computational approach to edge detection. *IEEE Transactions on pattern analysis and machine intelligence*, 8(6):679–698, 1986.
- [62] W Gray Jerome and Robert L Price. *Basic confocal microscopy*. Springer, 2018.
- [63] The University of Queensland. Confocal Microscopes. <https://imb.uq.edu.au/facilities/microscopy/hardware-software/confocal-microscopes>, September 29, 2017. [Online; accessed 06-March-2023].
- [64] Khuloud Jaqaman, Dinah Loerke, Marcel Mettlen, Hirotaka Kuwata, Sergio Grinstein, Sandra L Schmid, and Gaudenz Danuser. Robust single-particle tracking in live-cell time-lapse sequences. *Nature methods*, 5(8):695–702, 2008.
- [65] The Pandas development team. pandas-dev/pandas: Pandas. <https://doi.org/10.5281/zenodo.3509134>, February 1, 2020. [Online; accessed 09-November-2022].
- [66] John C Crocker and David G Grier. Methods of digital video microscopy for colloidal studies. *Journal of colloid and interface science*, 179(1):298–310, 1996.
- [67] C Bourges-Monnier and MER Shanahan. Influence of evaporation on contact angle. *Langmuir*, 11(7):2820–2829, 1995.
- [68] Álvaro G Marín, Hanneke Gelderblom, Detlef Lohse, and Jacco H Snoeijer. Rush-hour in evaporating coffee drops. *Physics of fluids*, 23(9):091111, 2011.
- [69] Meysam R Barmi and Carl D Meinhart. Convective flows in evaporating sessile droplets. *The Journal of Physical Chemistry B*, 118(9):2414–2421, 2014.